jmb Article

Mechanical Probes of SOD1 Predict Systematic Trends in Metal and Dimer Affinity of ALS-Associated Mutants

Atanu Das and Steven S. Plotkin

Department of Physics and Astronomy, *University of British Columbia, Vancouver, BC, Canada V6T 1Z1*

Correspondence to Steven S. Plotkin: *steve@physics.ubc.ca*
http://dx.doi.org/10.1016/j.jmb.2012.12.022
Edited by B. Honig

Abstract

Mutations and oxidative modification in the protein Cu,Zn superoxide dismutase (SOD1) have been implicated in the death of motor neurons in amyotrophic lateral sclerosis (ALS), a presently incurable, invariably fatal neurodegenerative disease. Here we employ steered, all-atom molecular dynamics simulations in implicit solvent to investigate the significance of either mutations or post-translational modifications (PTMs) to SOD1 on metal affinity, dimer stability, and mechanical malleability. The work required to induce moderate structural deformations as a function of sequence index constitutes a "mechanical fingerprint" measuring structural rigidity in the native basin, from which we are able to unambiguously distinguish wild-type SOD1 from PTM variants and measure the severity of a given PTM on structural integrity. The cumulative distribution of work values provided a way to cleanly discriminate between SOD1 variants. Disulfide reduction destabilizes dimer stability more than the removal of either metal, but not moreso than the removal of both metals. Intriguingly, we found that disulfide reduction mechanically stabilizes apo-SOD1 monomer, underscoring the differences between native basin mechanical properties and equilibrium thermodynamic stabilities and elucidating the presence of internal stress in the apo state. All PTMs and ALS-associated mutants studied showed an increased tendency to lose either Cu or Zn and to monomerize—processes known to be critical in the progression of ALS. The valence of Cu strongly modulates its binding free energy. As well, several mutants were more susceptible to loss of metals and monomerization than the disulfide-reduced or apo forms of SOD1. Distance constraints are required to calculate free energies for metal binding and dimer separation, which are validated using thermodynamic cycles. When distance constraints are removed, the results agree with those obtained from direct application of the Jarzynski equality.

Introduction

Copper, zinc superoxide dismutase (SOD1) is a homodimeric antioxidant enzyme of 32 kDa present in all eukaryotes. Each monomer consists of an eight-stranded Greek key β barrel of 153 amino acids [1–3] and binds one Cu ion and one Zn ion, which significantly enhance native thermodynamic and mechanical stabilities. [4,5]

Two large, functionally important loops determine the structure and activity of the enzyme. Loop VII or the electrostatic loop (residues 121–142) contains charged and polar residues that enhance enzymatic activity by inducing an electrostatic funnel toward the active site centered on the Cu ion, [6] which catalyzes the conversion of superoxide (O_2^-) to less toxic species (either O_2 or H_2O_2). Loop IV or the Zn-binding loop (residues 49–83) coordinates Zn with histidines 63, 71, and 80 and aspartic acid 83, which, along with a disulfide bond between cysteines 57 and 146, enforce concomitant tertiary structure in the protein. [7] Residues in the Zn-binding loop form about 38% of the dimer surface contact area so that disorder in the loop due to Zn expulsion and/or disulfide reduction can facilitate monomerization of the homodimer. [8–12]

The Cu on the other hand is coordinated by residues mainly in the β strands of the immunoglobulin-like core of the protein—histidines 46, 48, and 120, along histidine 63 that bridges the Cu and Zn ions—so that protein structure only weakly couples to Cu binding, [13,14] supporting a primarily enzymatic role of Cu.

Amino acid missense mutations at more than 150 positions in SOD1 have been found to cause amyotrophic lateral sclerosis (ALS), an invariably fatal neurodegenerative disease characterized by loss of the motor neurons in the brain, brainstem, and spinal cord.† Such familial mutations constitute about 20% of the cases of ALS known to display autosomal dominance,[15] conferring symptoms through a mechanism involving a toxic gain of function, in that SOD1 knockout mice do not develop the neurodegeneration indicative of the fALS (*f*amilial *ALS*)-like phenotype.[16] Gain-of-function symptoms have been variously attributed to generation of reactive oxygen and nitrogen species, cytoskeletal disruption, caspase activation, mitochondrial dysfunction, proteosome disruption, and microglial activation.[17–19] SOD-mediated fALS is one of the most prominent identified causes of the disease despite constituting only approximately 2–5% of all known cases. The vast majority, about 90%, of ALS cases have no known underlying etiology and are termed sporadic (sALS). Macroscopically, sALS is clinically indistinguishable from fALS.[20] Lewy-body-like inclusions in sALS have been found to be immunoreactive to SOD1-specific antibodies,[21] and misfolding-specific antibodies have also identified misfolded SOD1 protein in sALS inclusions.[22,23] At the molecular level, however, protease-resistant cores in aggregates as identified by matrix-assisted laser desorption/ionization–time-of-flight mass analysis were observed to differ between the wild-type (WT) sequence and the fALS-associated mutants G37R, G85R, and G93A,[24] which indicate that mutations can modulate structural polymorphism in aggregate cores, resulting in distinct physicochemical aggregate properties such as sequence-dependent solubility. The mutation-induced polymorphism of fibril cores has been recapitulated in coarse-grained simulations using discrete molecular dynamics with structure-based, Gō-like potentials.[25] Nevertheless, several studies have indicated that oxidative modification of WT SOD1 can be toxic in ALS, linking SOD1 misfolding to a common pathogenic mechanism in fALS and sALS.[26–30]

Studies involving misfolding-specific antibodies have shown that misfolded SOD1 (either G85R or G127X) can induce misfolding in natively structured WT SOD1 by direct protein–protein interactions.[31] Holo, pseudo-WT SOD1 (C6A/C111S) has been observed to aggregate under physiologically relevant conditions, with characteristics similar to aggregates in fALS patients.[32] Further, cell-to-cell transfer mediated by macropinocytosis has been observed in the fALS mutant H46R.[33] These studies point to prionogenic mechanisms for the propagation of SOD1 misfolding and aggregation—a common theme in protein-misfolding diseases.

SOD1 protein need not globally misfold or unfold in order to aggregate. Accumulated evidence for several proteins indicates that aggregation may be initiated from locally (rather than globally) unfolded states.[34] These partially disordered states may be induced by external agents or may become accessible via thermal fluctuations or rare events. For the case of SOD1, a near-native aggregation precursor was found for an obligate monomeric SOD1 variant (C6A/C111A/F50E/G51E), wherein protective cap regions are locally unfolded around the native β-stranded core.[35] As well, both crystal structures of the fALS mutants S134N and apo-H46R have been observed to adopt fibrillar structures with intercalating loops between largely native-like domains,[36] and S134N has been observed to form oligomers in solution that are stabilized by locally unfolded elements from the native structure, involving transient interactions between electrostatic loops from different dimers.[37]

The abovementioned studies have motivated a previous computational study, where we had focused on the native and near-native mechanical properties of WT SOD1, premature variants lacking post-translational modifications (PTMs), and both ALS-associated and rationally designed truncation mutants.[5] We felt that this approach was complimentary to experimental structural and thermodynamic assays. In that work, we examined relatively large changes in native structure as a result of significant perturbing mechanical forces; however, the forces are not so large as to induce global unfolding. The mechanical forces are applied across the whole protein surface to ascertain a "mechanical fingerprint" for a given SOD1 protein variant.

An all-atom, implicit solvent model was used, which in benchmark cases compared favorably to an explicit solvent model but less favorably with a structure-based Gō model. The (non-equilibrium) work values obtained by pulling a residue to 5 Å were found to strongly correlate ($r = 0.96$) with the equilibrium free-energy change for the same process, as calculated using the weighted histogram analysis method (WHAM). Thus, the work profiles obtained accurately represented the relative thermodynamic stability of various regions or the relative thermodynamic stability between mutant and WT for the same region.

We found that the mechanical profile of a given SOD1 variant could be best represented through the cumulative distribution of mechanical work values, where the work is obtained by pulling out various residues in the protein to a given distance. The cumulative distribution of work values can be thought of as a generalization of native "rigidity", which accounts for the fact that the rigidity can vary place to place, so that the collection of work values themselves obey a distribution that differs between SOD1 variants. For purposes of distinguishing cumulative work distributions of SOD1 variants, we saw that mechanical data collected for 48 residues were sufficient to represent more comprehensive sets of data, in that the cumulative work distribution

seemed to have converged to within ≈1 kJ/mol after a sample size of about 40 residues.

Mechanical fingerprinting studies of SOD1 variants with Zn-binding and electrostatic loops either truncated to Gly-Ala-Gly linkers[38] or extended by poly-glycine insertions revealed that, although the Zn-binding and electrostatic loops in apo-SOD1 destabilized the β-sandwich core of the protein in the absence of metals, evolution has responded by strengthening interactions in regions flanking the loops, in order to preserve the structural integrity of the core domain and presumably prevent misfolding. Nevertheless, mechanical fingerprinting studies of a series of C-terminally truncated mutants, along with an analysis of equilibrium dynamic fluctuations and solvent exposure while varying native constraints, together revealed that the apo protein is internally frustrated and that this internal strain is an allosteric consequence of evolution toward high metal-binding affinity; release of the stress in a truncation mutant causes loss of metal-binding function, even though all metal-binding ligands are still present.[5] Thus, the evolutionary optimization of SOD1 function as a metal-binding redox substrate competes with apo state thermo-mechanical stability, consequently increasing the susceptibility of misfolding in the apo state.

Here we examine mechanical properties of mutant and WT SOD1, as well as the free energetic changes accompanying PTMs such as metal binding and dimerization. The affinity for metals and dimer stability are determined by both WHAM and direct mechanical pulling assays using the Jarzynski equality, and the methods are checked for consistency. Of the 21 ALS-associated mutants investigated here, every one showed both reduced metal and dimer affinity. Some mutants had lower dimer affinity in the holo state than WT protein in the apo, disulfide-reduced state. PTMs such as disulfide reduction or metal depletion also lower dimer stability and metal affinity, for example, Cu depletion lowers the affinity for Zn and vice versa. Zn plays a larger role than Cu in determining the mechanical rigidity of the native state. Presence of the native C57–C146 disulfide bond induces stress in the apo state of the protein, which is relieved either upon metal binding or reduction of the bond. Thermodynamic quantities as obtained from our simulations are compared with those obtained experimentally in Discussion.

Results

The Jarzynski/Crooks equality overestimates the free-energy change due to conformational distortion

Figure 1a plots the work performed as a function of extension, for residue 25 of two SOD1 variants, (E,Zn) (Cu-depleted) SOD1 and (Cu,E) (Zn-depleted) SOD1. The protocol is described in Steered molecular dynamics simulations. Some variants have softer mechanical profiles than others; for residue 25, (Cu,E) is softer than (E,Zn). Figure 1b shows the work to pull the Zn ion to a given distance from its putative position in WT protein, along with the free energy as obtained from the WHAM method, as described in WHAM procedure for metal expulsion and dimer separation. Note that the free energy is not always less than the work for this trajectory—it is only when ensemble averaged that the thermodynamic inequality $F \leq \langle W \rangle$ holds. Both work and free energy begin to converge to their asymptotic values at distances beyond about 5 Å. Figure 1c shows the work to monomerize the WT dimer by pulling it apart, along with the free-energy change as obtained from the WHAM method. Note that the work performed is substantially larger than the free-energy change. Both work and free energy begin to converge to their respective asymptotic values after about 10 Å. The methods used for dimer separation are described in Steered molecular dynamics simulations and WHAM procedure for metal expulsion and dimer separation.

To calculate the free energy of local protein unfolding, metal expulsion, and dimer separation, we have calculated the work to either pull a particular C^{α} to 5 Å, pull a metal ion until the force drops to zero, or pull monomers in the dimer apart until the force drops to zero. The various assays are repeated multiple times, and the corresponding free-energy changes are obtained from the work values by applying the Jarzynski equality.[39–41] Finite sample-size corrections are accounted for,[42] as described in Free-energy differences from Jarzynski equalities and finite sample-size corrections.

The free-energy change is calculated from repeated pulling assays measuring the non-equilibrium work value to pull a residue to 5 Å, through the Jarzynski equality: $e^{-\Delta F/kT} = \langle e^{-W/kT} \rangle$. Here ΔF is the free-energy change, W is the work value, kT is Boltzmann's constant times the temperature in Kelvin, and the brackets $\langle \cdots \rangle$ denote the ensemble average over identical pulling assays.

The results are shown in Fig. 2: (a) and (b) show plots of the quantity $-kT \ln \langle e^{-W/kT} \rangle_N$, where the above ensemble average is evaluated over N trajectories (identical runs), as a function of the number of trajectories N. For sufficiently large N, the average should converge to the ensemble average. The plots in Fig. 2 indicate that about 14 trajectories are sufficiently large for convergence, for the pulling rates and extensions we considered in our study [red horizontal lines in (a) and (b) of Fig. 2].

Finite sample-size effects reduce the estimate for the free-energy change; however, the mean dissipated work in our pulling assays is modest, only about 1 kJ/mol, indicating that pulling is near equilibrium, and thus, finite sample-size corrections

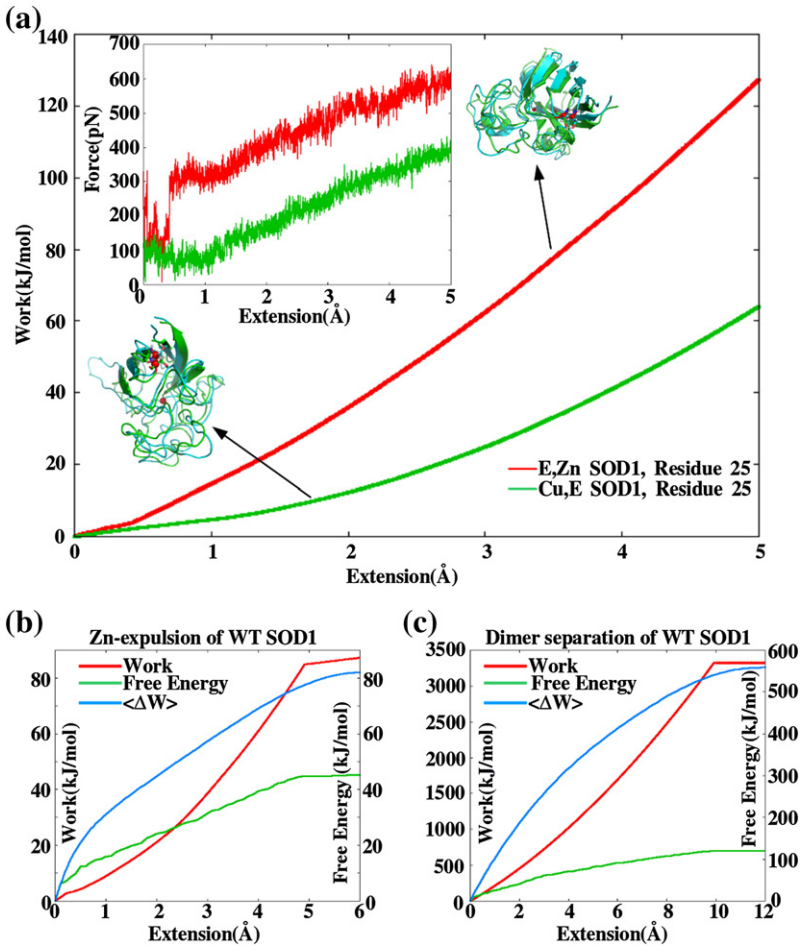

Fig. 1. (a) Work performed as a function of distance pulled. Tethers are placed at the C^{α} atom closest to the center of mass of the SOD1 monomer (H46) and the C^{α} atom of residue S25 of either (E,Zn) (red) or (Cu,E) (green) SOD1, in separate pulling assays. Inset of (a): force-extension profile of residue 25 for (E,Zn) (red) and (Cu,E) (green) SOD1. Ribbon representations of the protein are also shown; the tethering residue is shown in licorice rendering (in red) and the center C^{α} is shown as a red sphere. The initial equilibrated (at 0 Å, green ribbon) and final (at 5 Å, blue ribbon) structures are aligned to each other by minimizing RMSD; this indicates that, overall, the structural perturbation induced by pulling one residue to 5 Å is modest but significant enough to be unlikely thermodynamically based on the magnitude of the work values. (b) Work and WHAM-derived free energy to move Zn a given distance from its putative position in WT SOD1. Values have nearly converged after 5 Å. Note that the free energy is not always less than the work for a given trajectory (red); the thermodynamic inequality $\langle \Delta W \rangle > \Delta F$ only holds true after ensemble averaging, as seen for the blue curve representing the ensemble-averaged work (over 20 trajectories) to extend the metal to a given distance. (c) Work (red), average work (blue), and WHAM-derived free energy (green) to separate the WT SOD1 dimer by a given separation distance. Values have nearly converged after 10 Å. The free energy is substantially less than the work, much of which goes into conformational distortion of the protein when harmonic constraints on C^{α} atoms are not present.

are not large, about 1–3 kJ/mol [green horizontal lines in (a) and (b) of Fig. 2 give the refined estimate for the free-energy change accounting for finite sample-size corrections].

However, the free-energy changes obtained from this method are still larger than those of the WHAM method [blue horizontal lines in (a) and (b) of Fig. 2]. The discrepancy is about 0.6 kJ/mol when residue 10 is pulled to 5 Å and is about 5 kJ/mol when residue 17 is pulled to 5 Å. The reason is that pulling on a particular residue at a finite rate distorts the rest of the protein, and there is a free-energy change corresponding to this distortion that contributes to the total. The distortion may be avoided by applying constraints, but it is not obvious *a priori* how or where to apply such constraints when pulling residues away from the protein. The WHAM method minimizes the free-energy change due to distortion by equilibrating at each distance "window" in the corresponding umbrella potential. Convergence was tested by varying the number of windows between 25 and 40 and by varying the equilibration time within each window between 10 ns and 25 ns, for which the results did not noticeably change.

The free-energy changes for metal expulsion and dimer separation may also be calculated from both the Jarzynski equality and WHAM method. For these assays, distortion of the protein may be minimized by applying harmonic constraints to the C^{α} atoms of the protein. The harmonic constraints are applied in the WHAM analysis, and the results are compared with those of the (unconstrained) Jarzynski analysis. Side chains and other backbone atoms are allowed to move.

Perhaps the main concern is whether applying such constraints would impede the removal of the metal ion. The most direct, solvent-accessible pathway for metal expulsion was taken, as described in Tethering residues. To confirm that metal expulsion was not impeded by C^{α} atom constraints, we varied the stiffness of the C^{α} potential, from 0 (unconstrained) to 392×10^3 kJ/mol/nm^2, the stiffness of a single carbon–carbon bond, as used

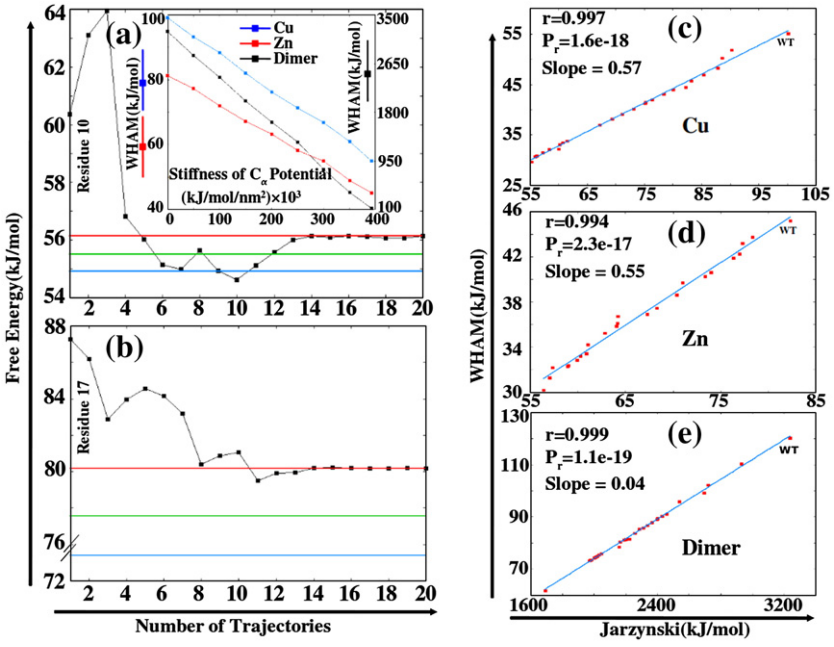

Fig. 2. Comparison of free-energy values calculated from Jarzynski's equality and from the WHAM. (a) Free energy as calculated using Jarzynski's equality, as a function of the number of repeated pulling assays or trajectories, for residue 10 to be pulled to 5 Å from its equilibrium position in a direction radially outward from the center of mass. (b) The same plot as (a) for residue 17. In (a) and (b), red horizontal line indicates the value of free energy calculated from the Jarzynski Eq. (2). The green line indicates the free energy obtained by accounting for extra corrections arising from finite sample sizes[42] described in Free-energy differences from Jarzynski equalities and finite sample-size corrections. The blue line indicates the free-energy value calculated by WHAM, wherein equilibration with umbrella sampling constraints allows conformational distortion to relax, see WHAM procedure for mechanical profiles. (c) Scatter plot of the free-energy values for Cu removal, as calculated by the Jarzynski Eq. (2) and WHAM with C^{α} constraints, for the mutants given in Table 1. WT protein in the upper right of the plot is indicated and has the largest binding free energy. The free-energy values strongly correlate between the two methods. (d) Same as (c) for the removal of Zn. (e) Same as (d) for the free energy of dimer separation. Note that although the free energies obtained by two methods strongly correlate, the slope of the best-fit line is much less than unity, indicating the presence of substantial additional free-energy changes due to conformational distortion using the Jarzynski method. [Inset to (a)] WHAM-derived free-energy changes for metal expulsion and dimer separation for WT holo-SOD1, as a function of the stiffness of the harmonic constraints on the C^{α} atoms. The rightmost points on each curve correspond to the WHAM free energies in (c)–(e), that is, at the values of harmonic constraint used to generate the WHAM free energies for those plots. The WHAM free energies at zero stiffness are consistent with the Jarzynski values of the free energy in (c)–(e).

in the WHAM method. If constraints impeded the process of metal expulsion, a minimum would be seen as a function of stiffness of the constraining potential. If constraints did not impede the process, the free energy *versus* the stiffness of the constraining potential would be monotonically decreasing.

The WHAM free energy of metal expulsion and dimer separation for the WT protein as a function of the stiffness of the constraining potential is plotted in the inset of (a) in Fig. 2. The free energy is indeed monotonically decreasing, indicating that the constraints do not impede the process of metal expulsion or dimer separation. The free energy of deformation may thus safely be minimized by applying such constraints, to obtain the direct free-energy cost of metal expulsion or dimer separation.

Figure 2c–e plots the free-energy changes for Cu expulsion, Zn expulsion, and dimer separation for the mutants of SOD1 given in Table 1. WHAM values are plotted on the ordinate; Jarzynski values, as given by Eq. (2) for 25 replicas (i.e., without any finite size corrections), are plotted on the abscissa. The unconstrained Jarzynski method overestimates the free-energy changes, for the reasons above. The slopes of the best-fit lines are all less than unity, and for dimer separation, the slope is particularly small. However, the correlations between the two separate methods are excellent, indicating that the deformation free energy is not a large and random component of the total free energy but likely correlates with the direct metal expulsion or monomerization free energy. For both Zn and Cu binding, the ratio of the binding free energies, Jarzynski to WHAM, is about 1.8. Relative rank ordering of the free energies between the WT sequence and mutants may be predicted either by the WHAM or by the Jarzynski method. We found, however, that the WHAM method was the most rapid and reliable way of determining free-energy changes in the system.

The rightmost data point in Fig. 2c–e refers to the WT protein (labeled), that is, the WT protein has the largest metal and dimer affinity. This is described in further detail below. Comparing the WHAM and Jarzynski values for, say, Cu expulsion in (c) of Fig. 2, we take the WHAM value of 55 kJ/mol from the value in the inset of (a) of Fig. 2 at C^{α} constraint of 392×10^{3} kJ/mol/nm^{2}, while the Jarzynski value of 100 kJ/mol is consistent with the unconstrained WHAM value of 99 kJ/mol in the inset of (a) of Fig. 2 (accounting for finite-size corrections to the Jarzynski estimate reduces the value by only about 0.3 kJ/mol). Thus, the WHAM values approach the

Table 1. Proteins considered for mechanical scan, metal affinity, and dimer stability estimation

Mechanical scan[a]/metal expulsion/monomerization	
SOD1 variant	PDB ID used for structure generation
WT holo	1HL5, 2C9V
(Cu,E)	2R27[b,c]
(Cu-shift,E)	2R27[b,c]
(E,Zn)	1HL4
apo(SH)[d]	1HL5, 1RK7[c]
apo[d]	1RK7[c]
holo(SH)	2AF2[c]
G127X	1HL5[e]
A4V	1UXM
D124V	3H2P
D125H	1P1V
D76Y	1HL5[e]
D90A	1HL5[e]
G37R	1AZV
G41D	1HL5[e]
G41S	1HL5[e]
G85R	2ZKW
G93A	3GZO
G93C	1HL5[e]
H43R	1PTZ
H46R	2NNX[c]
H46R/H48Q	2NNX
H80R	3QQD
I113T	1UXL
L144F	1HL5[e]
L38V	2WZ5
S134N	1OZU
T54R	3ECW
W32S	1HL5[e]

[a] Mechanical scans were performed for SOD1 variants above the horizontal line located between holo(SH) SOD1 and G127X.
[b] Missing regions in the PDB structure were remodeled as described in Remodeling disordered/missing regions in PDB structures.
[c] Structures reported have mutations from the WT sequence; these were "back-mutated" to construct structures for the WT sequence, as described in Remodeling disordered/missing regions in PDB structures and Modeling proteins with no PDB structure.
[d] Metal expulsion is not relevant for these variants.
[e] These mutants have no PDB structure reported, so are constructed by mutating the appropriate residues in PDB 1HL5.

Jarzynski values as the C^{α} constraints are removed and provide a satisfying consistency check.

ALS-associated SOD1 mutants show decreased affinity for both Cu and Zn

Copper and zinc ions were pulled out of their putative binding sites for the list of proteins given in Table 1. For mutant proteins with no Protein Data Bank (PDB) structure, the initial structure was generated by mutating the appropriate residues in the WT structure (PDB 1HL5) and equilibrating, according to Modeling proteins with no PDB structure. Some mutants of SOD1 are devoid of Cu in the PDB structure—these are H46R, H46R/H48Q, S134N, D124V, H80R, and D125H—and some are fully metal depleted: G127X and T54R.[31,43,44] For these proteins, metals were incorporated into the proteins by superposing them onto holo-SOD1. The metals were found to be metastable in their binding sites, that is, no forces were required to constrain the metals to their putative bound positions for the duration of the simulation.

The tethering residues are chosen according to Tethering residues, to select an easy pathway for metal expulsion; the other tethering point is the metal itself. From these pulling assays, 25 configurations were taken at separations between 0 and 5 Å and used as initial states in umbrella sampling, to obtain the free energy to extract the metal using WHAM.

The free-energy values of metal expulsion thus obtained are plotted in Fig. 3a and also given in Table S1. The values in Fig. 3a are sorted by decreasing Cu affinity, and the values in Table S1 are sorted by decreasing Cu affinity separately among mutants and WT PTM variants. The WT structure had both the highest Cu and the highest Zn affinity, with values of 53 kJ/mol and 40 kJ/mol, respectively.

The free energy obtained by the WHAM method accounts for solvation free energy (at the accuracy of the implicit solvent model) but not fully for the chemical potential of the unbound metal, which is a concentration-dependent quantity. The chemical potential must be taken into account in determining the probability a metal is bound. Nevertheless, it is clear that every mutation, whether or not the corresponding amino acid was near the binding site, decreased the affinity of the protein for the metals. A non-ALS-associated mutant, W32S, also reduced the affinity of the metals. The reduction in binding free energy from WT SOD1 is up to about 26 kJ/mol for Cu (T54R) and 15 kJ/mol for Zn (G127X). These reductions are due to the induced conformational strain at the binding site that arises from the resulting stresses of mismatching interactions after a mutation.

The free-energy values of Cu and Zn expulsion are highly correlated, that is, if the affinity of Cu was reduced, so was that of Zn. Three mutants stand out as exceptions: H46R, H46R/H48Q, and D125H. Residues 46 and 48 coordinate the Cu ion; thus, the Cu affinity is anomalously low in the corresponding mutants. The correlation coefficient between Cu^{2+} and Zn^{2+} binding free energies without these two mutants was 0.929, with significance $P_{\gamma}=4.4e-10$. The correlation coefficient between monovalent Cu^{1+} and Zn^{2+} binding free energies without these two mutants was $r=0.930$, with significance $P_{\gamma}=3.7e-10$. The mean occupation numbers of Cu and Zn for several SOD1 mutants have been obtained experimentally by Hayward *et al.*[45] Re-analyzing this data to inspect the correlation between Cu and Zn content gives a correlation of $r=0.87$ ($p=5e-6$), $r=0.84$ ($p=1e-4$) if mutants H46R, H48Q, and D125H are removed. The strong effect of D125H on Cu

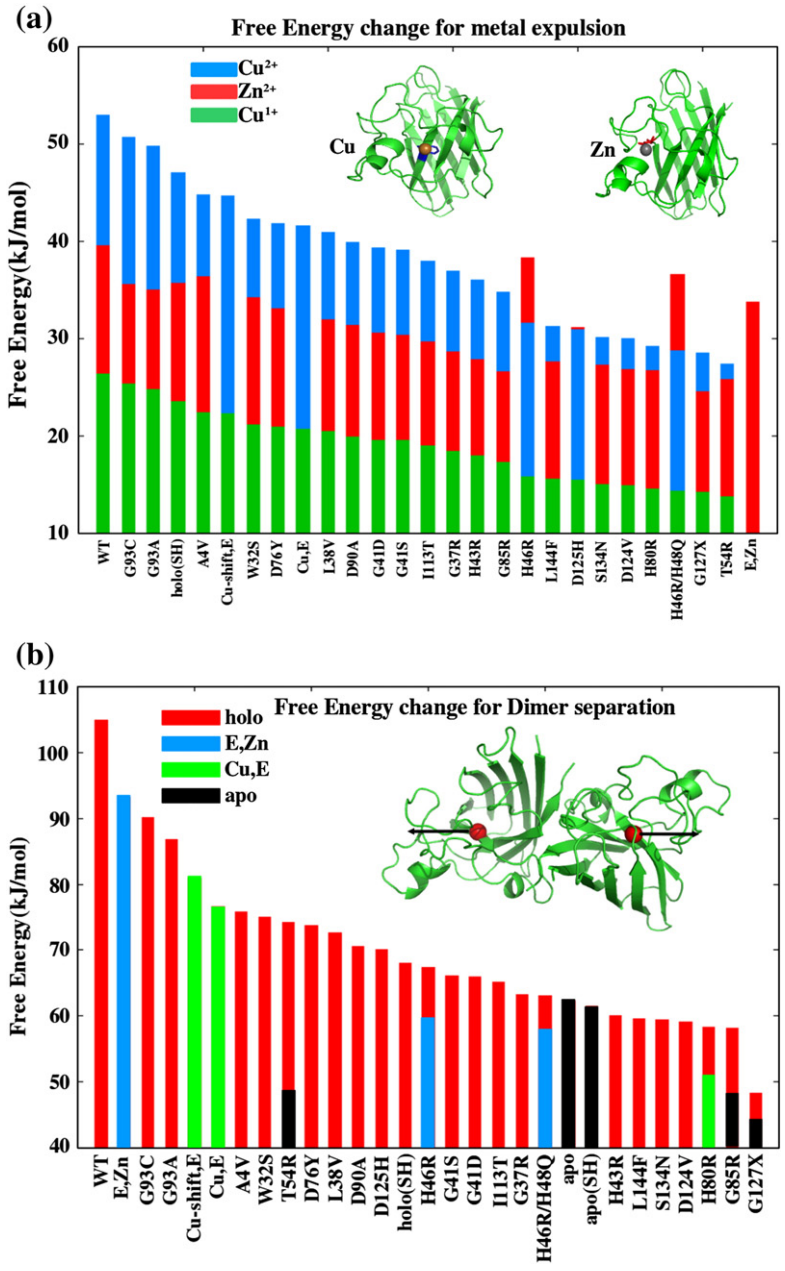

Fig. 3. (a) Free energy of copper (Cu) and zinc (Zn) binding/expulsion for WT SOD1 and mutants, sorted by decreasing Cu affinity. Binding free energies are obtained using WHAM as described in WHAM procedure for metal expulsion and dimer separation. Blue bars indicate Cu binding free energy, red bars indicate Zn binding free energy, and green bars indicate monovalent Cu^{1+} binding free energy. The heights of all bars start from zero. This binding energy accounts for solvation free energy at the level of the implicit solvent model. Inset images are intended to depict the direction of the pulling pathway, which was chosen as the direction with the most immediate solvent exposure. Metals are shown as an orange sphere for Cu and as a gray sphere for Zn, and the tethering residue used in the pulling simulations is color coded directly behind it. For Cu expulsion, this was residue 45 (blue cartoon), and for Zn expulsion, this was residue 83 (red cartoon). (b) Free energy to monomerize a homodimer of various SOD1 species. Both ALS-associated mutants and variants lacking PTM (metal depleted or disulfide reduced) are considered. Free energies are rank ordered strongest to weakest: holo-SOD1 has the strongest binding free energy, and G127X has the weakest. All mutants and variants showed weaker dimer stability than holo WT SOD1. The free energy to separate the dimer into monomers is obtained using WHAM. The inset shows a ribbon representation of the monomers constituting the dimer. The tethering residues, $C^{\alpha}(46)$ on each monomer, are shown as red spheres, and the direction of pulling used to generate initial conditions in WHAM is indicated by arrows. All mutants are taken in the holo form, with Cu and Zn in their putative binding positions. As well, H46R and H46R/H48Q do not bind Cu, H80R does not bind Zn, and G127X does not bind either metal; in these cases, we also calculated the binding free energy for the appropriate metal-depleted forms. From (a), the Cu affinity for the T54R variant was the lowest of all mutants, and the Zn affinity was the second lowest after G127X—lower than H80R that does not bind Zn. For these reasons, we also calculated the free energy to monomerize apo T54R dimer.

affinity is more subtle and involves propagation of strain through the native protein; further description of the effect is given in Discussion.

SOD1 catalyzes the disproportionation of superoxide anion (O_2^-) in a two-step reaction, wherein the Cu cation cycles between divalent and monovalent states. In the monovalent state, the binding affinity for Cu^+ is reduced by slightly more than a factor of 2, resulting in more likely release of the cation, particularly for mutants. In fact, affinities for monovalent Cu^+ were always less than those of Zn^{2+}, indicating ready release of monovalent Cu upon structural perturbation or rare thermodynamic fluctuation.

We have further checked that metal depletion and monomerization each satisfy a thermodynamic cycle, such that, upon metal re-insertion or re-dimerization, along with re-equilibration after the respective process, the net free-energy change over

the cycle is zero within the errors of the simulations. The thermodynamic cycles are shown schematically in Fig. 4, and the free-energy changes for the respective processes are tabulated in Table S2. On average, $\sum_{cycle}\Delta F_i \approx 0.15$ kJ/mol for metal expulsion/insertion and $\sum_{cycle}\Delta F_i \approx 0.2$ kJ/mol for monomerization/dimerization, for the cases that we benchmarked.

ALS-associated SOD1 mutants show increased tendency to monomerize

Dissociation of the native SOD1 dimer is a prerequisite for its aggregation.[10,46,47] The pathway to aggregation generally proceeds by nonnative dimer formation and subsequent oligomer formation. We investigated how both mutational modification and PTM modified dimer stability, for the ALS-associated mutants and PTM variants of SOD1 given in Table 1.

Using the WHAM methodology described in WHAM procedure for metal expulsion and dimer separation, we found the free energy to separate the homodimer into a pair of monomers. A plot of the dimer binding free energies, rank ordered from strongest to weakest, is shown in Fig. 3b. The absence of any PTM (e.g., absence of a metal or reduction of the disulfide bond) lowered the free energetic stability of the dimer. All ALS-associated holo mutants had reduced dimer stability, and several that we investigated had less dimer stability than that of apo(SH) WT, which is known to monomerize.[11] On the other hand, apo(SH) WT SOD1 had lower dimer stability than 15/22 holo ALS-associated mutants. The non-ALS-associated mutant W32S showed reduced dimer stability. G127X, an obligate monomer in *in vitro* studies,[31] had the lowest dimer stability: a significant fraction of the residues participating in the dimer interface is removed by the terminal sequence mutation.

The trend in dimer stability did not correlate with the proximity of a mutated residue to the dimer binding interface, by measuring either the distance to the closest residue in the binding interface ($r=0.15$, $P=0.51$) or the mean distance to residues putatively involved in the dimer interface: residues 4, 50–53, 114, 148, and 150–153 ($r=0.096$, $P=0.67$). These results support a dimer destabilizing mechanism by mutations that involves the long-range propagation of stress through interaction networks in the protein, an interpretation that is consistent with previous experimental[48] and simulation studies.[49]

Metal depletion weakens the mechanical stability of WT SOD1—zinc moreso than copper

To investigate the effect of the presence or absence of Cu and Zn ions on the mechanical stability of WT SOD1, we examined the mechanical profiles of the metal present (holo), Cu-depleted (E, Zn), Zn-depleted (Cu,E), Zn-depleted form with Cu shifted to the Zn position (Cu-shift,E), and metal-

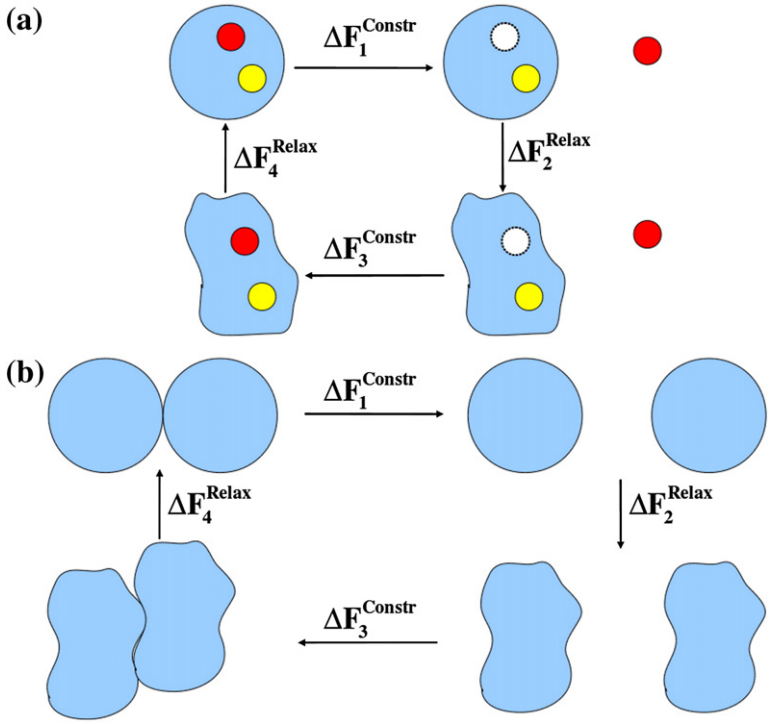

Fig. 4. Schematic representations of the thermodynamic cycles associated with metal extraction and dimer separation of SOD1 variants. (a) Free-energy changes associated with different steps of the metal-expulsion/metal-insertion thermodynamic cycle. Cu and Zn ions are shown as yellow and red spheres. ΔF_1^{constr} is the free-energy change for metal expulsion from the protein with the C^{α} constraints present (see the text); ΔF_2^{constr} is the free-energy change associated with the relaxation process where the constraints were gradually removed after metal expulsion; ΔF_3^{constr} is the free-energy change of inserting the same metal back into the half-metallated protein, with C^{α} constraints present to preserve its initial backbone conformation; and ΔF_4^{relax} is the relaxation free energy after metal insertion. The sum of the free-energy changes around the thermodynamic cycle is zero within the errors of the simulation, validating the calculation of expulsion free energies. (b) Same as (a), only here the free-energy changes refer to monomerization or dimerization compared to metal expulsion or metal insertion in (a).

depleted (apo) forms of SOD1. Mechanical profiles were obtained from pulling simulations as described in Steered molecular dynamics simulations. Inset (a) of Fig. 5 shows the mechanical profiles of all the above variants except for apo-SOD1 (an analogous figure including the data for apo-SOD1 is given in Fig. S1).

The work values in the mechanical profile are significant compared to thermal energies, ranging from about $16k_BT$ to $56k_BT$. Though the structural perturbations are fairly modest in comparison to global unfolding, the energetics of the pulling process is sufficiently non-perturbative that the work values across the set of 48 residues used here do not correlate with the RMSD values for the respective residues (see Table S3).

The mechanical profiles are significantly different for all the variants—a table providing the cross-correlation coefficients is given on the left of Fig. 5, as well as in Table S4, which shows that no mechanical profiles is well correlated with any other. It is worth noting, however, that the correlation coefficients, though weak, are statistically significant between some variants: the *p*-value between (Cu,E) and (Cu-shift,E) is 0.015, and the *p*-value between holo and (Cu-shift,E) is 0.028. The effect of demetallation is difficult to discern from the mechanical profiles in inset (a). Here the cumulative distribution proves to be valuable in elucidating the mechanical discrepancies between SOD1 variants and is shown in the main panel of Fig. 5. The probability distribution of work values can differentiate work profiles for different SOD1 species [inset (b) of Fig. 5], but unlike the cumulative distribution, it requires binning and does not discriminate variants as clearly as the cumulative distribution.

According to the cumulative distributions in Fig. 5, metal depletion mechanically destabilizes the protein. That is, after depletion of either Cu or Zn, the protein is more mechanically susceptible to perturbing forces. The distribution of apo-SOD1 is broadened compared to (Cu,E) SOD1, but not overall weakened (Fig. S1). The relative importance of Cu and Zn in determining the mechanical rigidity of the protein can also be ascertained. Zn depletion results in more destabilization than Cu depletion does, over the whole range of work values observed (green and blue curves in Fig. 5). That is, at any given perturbing work value, more residues in the (Cu,E) protein would be substantially disordered than in the (E,Zn) protein. Equivalently, say, for the weakest one-third (or any fraction) of the residues, a smaller value of work is required to substantially disorder those residues in the (Cu,E) variant than in the (E,Zn) variant. Note that the residues in the weakest one-third may be different in the two variants.

The loss of Cu and/or Zn destabilizes both the Zn-binding loop and the electrostatic loop, Zn moreso than Cu. Zn has close proximity to some of the residues in the electrostatic loop and is also involved

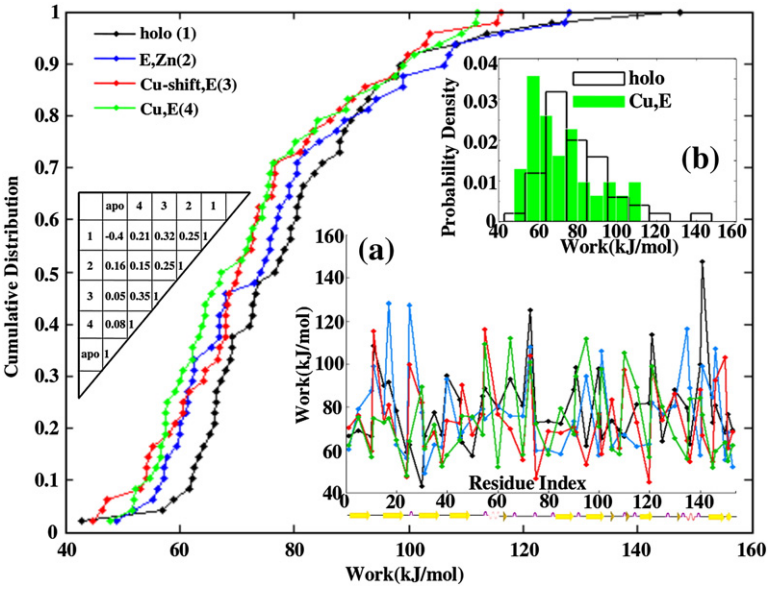

Fig. 5. The effect of metal depletion on the mechanical stability of SOD1. (Inset a) Mechanical profiles of holo-SOD1 (black), (E,Zn) SOD1 (blue), (Cu,E) SOD1 (green), and (Cu,E) SOD1 with the Cu ion shifted from its putative position to that of the Zn (red), which is the location of the metal observed in the crystal structure of PDB 2R27.[7] Profiles are color coded according to the legend on the upper left. The effect of metal depletion modulates the entire mechanical stability profile. Work values for individual residues are given in Table S5. (Inset b) Probability distributions of mechanical stability for holo and (Cu,E) variants. This representation shows that the distributions are indeed different; however, there is significant overlap, which along with the necessity of binning the data to construct the histogram makes the differences difficult to quantify. (Main panel) Cumulative distributions of the above SOD1 variants. The cumulative distribution requires no binning and simply rank orders and accumulates the work values. With the use of this representation, discrepancies between work profiles most clearly emerge. The mechanical stability of the SOD1 variants can be rank ordered, strongest to weakest, as holo, (E,Zn), (Cu-shift,E), and (Cu,E). Also shown in the main panel is a correlation matrix resulting from a pairwise comparison of the work values for all pairings of SOD1 variants. The profiles do not correlate, again supporting the notion that metal depletion modulates the entire mechanical stability profile. A similar plot also containing the cumulative distribution for apo-SOD1 is given in Fig. S1.

in helix dipole capping interactions with helix 133–138.[50] From the work values in the mechanical profiles (see Table S5), the mean work for residues in the mechanical scan that were in the Zn-binding loop (residues 50, 54, 55, 60, 65, 70, 73, 75, and 80) was 83.9 kJ/mol for holo, 78.2 kJ/mol for (E,Zn), 76.4 kJ/mol for (Cu,E), and 71.5 kJ/mol for apo. The mean work values for the corresponding residues in the electrostatic loop (residues 121, 125, 130, 135, 136, 140, and 141) was 93.5 kJ/mol for holo, 85.6 kJ/mol for (E,Zn), 77.7 kJ/mol for (Cu,E), and 72.9 kJ/mol for apo. The changes in work values with respect to holo-SOD1 are largest for the zinc binding and electrostatic loops (Fig. S7), indicating that the mechanical stability of these regions is preferentially dependent upon metal content. This finding is supported by dynamical fluctuation data, which show preferential increase in root-mean-square fluctuation values for the zinc binding and electrostatic loops (Fig. S7 and Table 2).

The changes in the mechanical stability profiles as a function of sequence index, when metals are removed, are subtle to predict and would likely involve a detailed quantification of the network of interactions throughout the protein. The modulus of the changes in work values do not correlate with simple parameters such as distance to the either metal (all correlation coefficients had $r<0.26$).

In the crystal structure of (Cu,E) SOD1, Cu resides near the putative Zn position. We tested whether this shift in position lowered the free energy by pulling the Cu from its putative position in the crystal structure to the Zn binding position and by applying umbrella sampling with the WHAM method as described in WHAM procedure for shifting Cu to the Zn binding position, to obtain the free-energy change for such a shift. Indeed, these simulations gave a reduction in free energy of −5.7 kJ/mol, indicating that the Zn binding position is more favorable for the Cu ion, when only Cu is bound. However, the free-energy barrier between the Cu and Zn binding positions is sufficiently large, about 8 kJ/mol, that we did not see the Cu change binding positions during the course of our simulations (covering 0.2 μs) when Zn was absent. We tested the hypothesis that the shift of Cu also mechanically stabilizes the protein, by calculating the mechanical profile and cumulative distribution of (Cu-shift,E) SOD1. These results are shown in Fig. 5, and the values are given in Table S5. Shifting of the Cu ion to the Zn position significantly increases in the mechanical stability of the protein: The probability to obtain, by chance, a distribution as stable or more stable than the (Cu-shift,E) distribution from the (Cu,E) distribution is $\approx 1.4e-7$ (see Statistical analysis and Fig. S2). As mentioned above, the work profiles of (Cu,E) and (Cu-shift,E) SOD1 are only weakly correlated: $r=0.35$, $p=0.015$ (correlation table in Fig. 5). Shift of the Cu to the Zn position globally changes the mechanical malleability of the protein.

The work profiles of both (Cu,E) SOD1 and (Cu-shift,E) SOD1 show lower stability in the metal-binding residues H80 and H120, compared to holo-SOD1. The work values for residue 120, which coordinates the Cu^{2+}, are 81.6 kJ/mol in the holo state, 56.6 kJ/mol in the (Cu,E) state, and 44.7 kJ/mol in the (Cu-shift,E) state. That is, Zn depletion destabilizes Cu-binding residue 120, and shift of the Cu ion to the Zn binding position further destabilizes that residue. Similarly, the work values for residue 80, which coordinates Zn^{2+}, are 73.1 kJ/mol in the holo state, 57.6 kJ/mol in the (Cu,E) state, and 68.6 kJ/mol in the (Cu-shift,E) state. That is, Zn depletion destabilizes coordinating residue H80, and shift of the Cu to the Zn position, a free energetically favorable process, partially recovers the mechanical stability of that residue in the WT protein.

The distribution of apo-SOD1 is broadened compared to (Cu,E) SOD1, but not weakened overall (the mean work for both variants was within 0.2 kJ/mol). That is, the most weakly mechanically stable residues in apo-SOD1 are less stable than the weakest mechanically stable residues in (Cu,E) SOD1 (though these residues are not the same), but the most stable residues of apo-SOD1 are more stable than the most stable in (Cu,E) SOD1 (and these residues are also not the same in the two variants).

Metal binding and disulfide bonding are cooperative: removing one destabilizes the other

Figure 6 plots the cumulative distributions of the mechanical work profiles for holo, apo, holo/SS-reduced [holo(SH)], and apo/SS-reduced [apo(SH)] SOD1. All modifications destabilize holo-SOD1. By comparing apo with holo(SH) SOD1, however, metal depletion has the largest destabilizing effect with only a few exceptions, over the bottom 77% of the work values. The cumulative distributions then cross at around 81 kJ/mol.

The weakest regions, with work values less than 60 kJ/mol, are on average about 5 kJ/mol weaker in apo-SOD1 than in holo(SH) SOD1, while the residues with moderate mechanical stability in the range 60–80 kJ/mol are only about 1.4 kJ/mol weaker on average for apo-SOD1. In this regime, disulfide reduction has nearly as much destabilizing effect as metal depletion. The most mechanically stable regions, with work values >86 kJ/mol, are on average about 5.5 kJ/mol weaker for holo(SH) SOD1 than for apo-SOD1, that is, disulfide reduction is more destabilizing for the most mechanically stable residues requiring the highest work values. It is worth emphasizing again that these regions in the cumulative distribution need not involve the same residues for the two variants.

Table 2. Experimental validation and predictions of the model

Property	Simulation	Experimental reference
ΔG of apo WT dimer→apo monomer	62 kJ/mol (Fig. 3b)	61 kJ/mol[51a]
ΔG of apo G85R dimer→apo monomer	47.9 kJ/mol (Fig. 3b)	48.9 kJ/mol[48]
Nonlocal destabilization of dimer stability of SOD1 mutants	Fig. 3b (and the text)	Refs. 48 and 49[b]
Zn-binding ΔG for WT SOD1	40 kJ/mol (Fig. 3a)	40 kJ/mol,[46] 45 kJ/mol,[52c] 56 kJ/mol,[12] 76 kJ/mol[53]
Cu-binding ΔG for WT SOD1	53 kJ/mol (Fig. 3a)	98 kJ/mol[53]
Zn-binding $\Delta\Delta G$ for mutant SOD1 [value(mutant)], $r=0.99$, $p=0.01$	3.2 kJ/mol (A4V), 4.6 kJ/mol (G93A), 7.7 kJ/mol (L38V), 12.3 kJ/mol (S134N)	−2.9 kJ/mol (A4V), −1.7 kJ/mol (G93A), 2.9 kJ/mol (L38V), 6.7 kJ/mol (S134N)[12]
Cu-binding $\Delta\Delta G$ for mutant SOD1 [value(mutant)], $r=0.78$[d]	8.1 kJ/mol (A4V), 14.9 kJ/mol (I113T), 12.0 kJ/mol (I38V)	1.2 kJ/mol (A4V), 2.1 kJ/mol (I113T), 2.4 kJ/mol (L38V)[53]
(Cu,E) SOD1 is more malleable than (E,Zn) SOD1 (Zn binding facilitates native structure moreso than Cu binding)	Fig. 5	Refs. 36 and 54–57
Zn-binding and electrostatic loops are selectively destabilized by metal release	Fig. S7	Refs. 7, 13, 14, 36, and 57
apo(SS) is less stable than holo(SH) SOD1	Fig. 6, Fig. S6, Table S5	Ref. 58
Validation of Jarzynski equality with WHAM for native mechanical stability	Fig. 2	Ref. 42

Predicted property	Simulation	Suggested experiment
Dimer stability for SOD1 variants and ALS mutants[e] (all had reduced ΔG w.r.t. WT; D124V, H80R, and G85R were among lowest)	Fig. 3b	Equilibrium denaturation
Zn-binding/Cu-binding ΔG for SOD1 variants and ALS mutants[f] (all had reduced ΔG w.r.t. WT; T54R was among lowest; D125H has comparable Cu and Zn affinities)	Fig. 3a	Chelation assay, inductively coupled plasma mass spectroscopy (ICP-MS)
Correlation between Zn-binding and Cu-binding ΔG values	Fig. 3a and the corresponding text $r=0.93$, $p=4e-10$	ICP-MS, chelation assays [in Ref. 45, $r=0.87(0.84)$, $p=5e-6(1e-4)$[g]]
Quantitative valence dependence of Cu affinity; Cu^{1+} has lower affinity than Zn	Fig. 3a	Competitive chelation (see, e.g., Ref. 59)
Larger effect of Zn on Cu affinity than Cu on Zn affinity	Fig. 3a	ICP-MS, chelation assays
The putative Zn-binding site is more favorable for Cu (Cu binding is under kinetic control); kinetic barrier separates binding sites	Metal depletion weakens the mechanical stability of WT SOD1—zinc moreso than copper	EXAFS; relative occupation of Cu- and Zn-binding sites in crystal structures in absence of Zn
Shift of Cu- to Zn-binding site stabilizes SOD1 relative to (Cu,E) SOD1	Fig. 5	AFM/optical trap or DSC of E,Cu SOD1, derived perhaps by chelation
Cooperativity between metal binding and disulfide formation	Fig. 6	AFM/optical trap with chelator (DTPA)/reductant (TCEP)
Strain/frustration in the apo state	Fig. 6, Table S5 (holo/apo)	Relaxation dispersion NMR, hydrogen/deuterium exchange
Nonlocal effects of mutations or metallation state on mechanical stability	Fig. 5, Fig. S1	Multiple-tethering-point AFM or optical trap probes of SOD1
Mechanical stabilization of apo(SH) SOD1 with respect to apo(SS) SOD1	Fig. 6	AFM/optical trap[h]
Cu,E(SS) SOD1 is marginally less (mechanically) stable than holo(SH) SOD1	Fig. S6, Table S5	DSC, equilibrium denaturation; Chevron kinetics (AFM/optical trap)

[a] Dimer binding free energies for pseudo-WT C6A/C111S are somewhat less, about 51–52 kJ/mol per dimer.[48,51,60]
[b] Simulation result.
[c] This number is reported as an approximate lower bound to the affinity.
[d] Data set is too small ($N=3$) for the correlation to have statistical significance.
[e] Mutants with newly predicted dimer binding free energies: holo(SH), (Cu-shift,E)(SS), Cu,E(SS), E,Zn(SS), and E,Zn(SH); the following apo mutants: T54R, H80R, and G127X; and the following holo mutants: A4V, G37R, L38V, G41D, G41S, H43R, H46R, H46R/H48Q, T54R, D76Y, H80R, G93C, I113T, D124V, D125H, G127X, S134N, and L144F.
[f] Mutants and variants with predicted metal binding free energies for Zn: holo(SH), E,Zn(SS), E,Zn(SH), W32S, G37R, G41D, G41S, H43R, H46R, H46R/H48Q, T54R, D76Y, H80R, G85R, G93C, D124V, D125H, G127X, and L144F; for Cu: holo(SH), (Cu-shift,E)(SS), Cu, E(SS), W32S, G37R, G41D, G41S, H43R, H46R, H46R/H48Q, T54R, D76Y, H80R, G85R, G93A, G93C, D124V, D125H, G127X, S134N, and L144F.
[g] Proteins used: WT, A4V, L38V, G41S, G72S, D76Y, D90A, G93A, E133Δ, H46R, H48Q, G85R, D124V, D125H, and S134N (numbers in parentheses do not include H46R, H48Q, and D125H).
[h] The fact that NMR measurements report no significant change in tertiary structure upon disulfide reduction of monomeric apo(SS) SOD1[8] is consistent with this prediction.

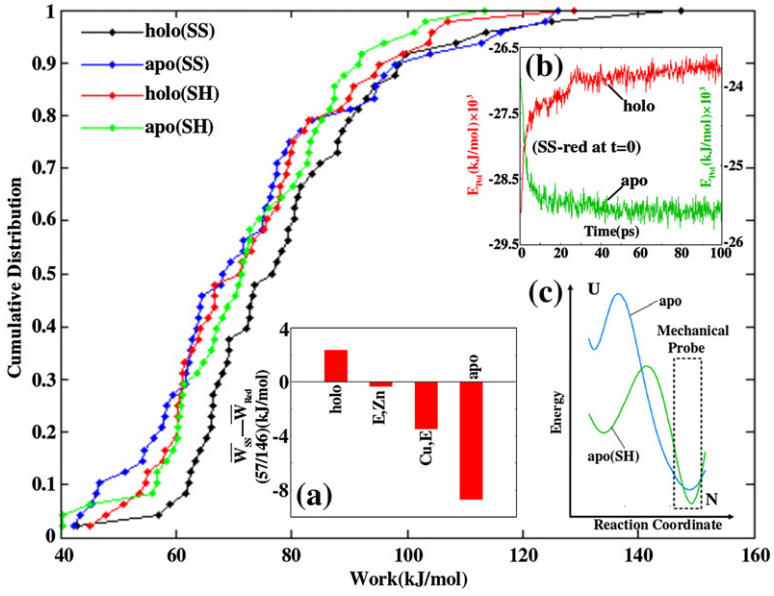

Fig. 6. Interplay of disulfide linkage and metal depletion on protein stability. (Main panel) Cumulative distributions of work values for holo, apo, holo(SH), and apo(SH) SOD1. Both metal depletion and disulfide reduction reduce the stability of the WT protein, but metal depletion generally results in larger destabilization for work values less than about 80 kJ/mol. Comparison of the holo, holo(SH), apo, and apo(SH) cumulative distributions indicates that the presence of the disulfide bond stabilizes the holo form of SOD1 but destabilizes the apo form of SOD1. (Inset a) Bar plot of work differences for several SOD1 variants using the following procedure. We first found the average work, $\overline{W}$, to pull residues 57 and 146 to 5 Å, for both disulfide-containing and disulfide-reduced forms of holo, (E,Zn), (Cu,E), and apo (metal-depleted) SOD1. Then we took the difference in average work between the disulfide-present and disulfide-reduced forms for all those variants $\overline{W}_{\text{“SS”}} - \overline{W}_{\text{“Red”}}$. This was taken as a measure of effect of disulfide bond on the stability of SOD1. The disulfide bond stabilizes the holo form but destabilizes the (Cu,E) and apo forms. (Inset b) Potential energy as a function of time after initial reduction of the disulfide bond at $t=0$. Red curve is for holo-SOD1, and green curve is for apo-SOD1. (Inset c) Schematic free-energy profiles of apo and apo(SH) SOD1 (see Discussion). The key features of the profiles are a stiffer native basin, a moderately lower free energy in the native state, and a substantially lower free energy in the unfolded state, for apo(SH) SOD1 relative to apo-SOD1. The mechanical profiles probe the region outlined in the dashed box.

Perhaps surprisingly, metal depletion appears to have a moderately stabilizing effect on holo(SH) SOD1, at least over the range of work values less than 81 kJ/mol. Apo(SH) SOD1 contains the three weakest residues between the holo(SH) and apo(SH) variants; however, for 19 out of the total of 31 residues of the mechanical scan with work values less than 81 kJ/mol, apo(SH) SOD1 is more stable than holo(SH) SOD1. This is seen directly from the cumulative distributions. This observation prompted a study of the mechanical rigidity of SOD1 variants in the vicinity of the residues involved in the disulfide bond, for various metallated states. For a given metallated state of the protein, we recorded the mean mechanical work to pull residues 57 and 146 (involved in the disulfide bond) to 5 Å, for both the disulfide-present state and the disulfide-reduced state. If the disulfide bond is present, both residues will tend to move together when one is pulled. Inset (a) of Fig. 6 plots the difference, SS-present minus SS-reduced, of the mean mechanical work to pull residues 57 and 146, for holo, (E,Zn), (Cu,E), and apo-SOD1. For holo-SOD1, the presence of disulfide bond results in mechanical stabilization of these residues or stronger coupling to the rest of the protein. The effect goes away once Cu is removed from the protein. If Zn is removed, the reverse effect is observed: formation of the disulfide bond weakens the mechanical coupling between residues 57/146 and the rest of the protein. The mechanical weakening effect of the disulfide bond is most significant in the apo state of the protein.

Just as metal depletion mechanically stabilizes the disulfide-reduced state of the protein, so also does disulfide reduction stabilize the metal-depleted protein. Comparing the cumulative distributions of apo(SS) and apo(SH) SOD1, 32 of 38 work values less than 86 kJ/mol are more stable for apo(SH) than for apo(SS). Thus, disulfide reduction mechanically stabilizes at least the weaker regions of the apo protein.

What about the effect on the overall potential energy in the protein? We considered the following kinetics study: in both holo-SOD1 and apo-SOD1, we instantaneously reduced the disulfide bond and investigated the potential energy in the protein as a function of time. Inset (b) of Fig. 6 plots the potential energy as a function of time immediately after disulfide reduction, for the holo protein (red) and the apo protein (green). The holo protein indeed shows an increase in potential energy indicating a destabilizing effect due to disulfide reduction. However, consistent with the above observations from the cumulative distribution and the local work on disulfide-participating residues, the potential energy in the apo protein decreases with time after reduction. This indicates that the presence of the disulfide bond strains the apo protein, and the potential energy in the protein is thus lowered by its reduction.

The converse study of removing metals from the protein with the disulfide bond either present or

absent is contained in Fig. 3a and Table S1. The holo(SH) protein has moderately reduced affinity for Cu and Zn, by about 5.9 kJ/mol and 3.9 kJ/mol, respectively. Thus, reducing the disulfide bond lowers the affinity for the metals, and removing the metals changes the effect of disulfide bond formation from protein stabilizing to protein destabilizing.

Discussion

Operating on the premise that ALS-associated mutant sequences of SOD1 protein had different mechanical properties than the WT protein, we have undertaken a computational study to probe these mechanical differences. By employing a combination of pulling simulations and umbrella sampling with the WHAM, we can computationally investigate disease-relevant misfolding processes such as loss of native structure, metal loss, and monomerization of native dimers. We found the likelihoods of these processes to be significantly greater in ALS-associated mutant proteins, supporting the idea that although the consequences for folding thermodynamic stability of many ALS-associated mutants may be modest,[45,61] the effects on dimer stability and metal affinity can be large. The commonly used monomeric F50E/G51E mutant provides a clear precedent for such effects. Moreover, dimer and metal affinities can be influenced in subtle ways: mutations distant from the Zn or Cu can have large effects on metal affinity, and mutations far from the dimer interface can have large effects on dimer stability.

Mechanical probes were employed by simulating tethers on the center residue of SOD1 and on various residues on the protein surface. The experimental analogue to such an *in silico* approach would require multiple AFM (*a*tomic *f*orce *m*icroscopy) or optical trap assays involving numerous residue pairs about the protein surface as tethering points. This is difficult and time consuming to achieve in practice, which thus provides an opportunity for the present simulation approaches. Such a study of the native surface malleability for mutants of SOD1 may be relevant in understanding the process of intermolecular transmission of misfolding in the cell.[31]

The work to pull a given residue to a distance sufficient to constitute an anomalously large fluctuation, for example, 5 Å, can be calculated as a function of sequence index for a given SOD1 variant. This results in a characteristic mechanical profile for that protein. We found that such a profile was significantly different between WT SOD1 and other PTM variants such as metal-depleted or disulfide-reduced SOD1. A systematic comparison of mechanical profiles between WT SOD1 and ALS-associated mutants is an interesting and important future study.

Some of our *in silico* observations are consistent with previous experimental benchmarks; however, we have also made several new observations here that are experimentally testable. Table 2 gives a summary of the experimentally validated results in this paper, as well as the main experimentally testable predictions contained in the paper. We elaborate on the entries in this table in the discussion below.

A given PTM globally modulates the mechanical profile, inducing both local and nonlocal changes in stability. These changes can be destabilizing in some regions and stabilizing in others. Understanding such stability changes well enough to predict them is a difficult challenge and would involve quantifying the interaction networks throughout SOD1 and how these networks transmitted stresses when one region of the protein was strained. A detailed study of the consequences of such mutations, for example, by studying the long-range communication through interaction networks in the mutant *versus* WT protein (see, e.g., Khare and Dokholyan[49]), is an interesting topic of future research.

The free energy to remove metals or monomerize SOD1 variants may be calculated using WHAM. For these processes, harmonic distance constraints between C^{α} atoms were applied to prevent the inevitable structural deformations that occur in such a non-equilibrium pulling assay, which would add to the measured free energy. The free energy as obtained from the Jarzynski equality (without distance constraints) was thus always greater than the free energy obtained from the WHAM protocol along with harmonic distance constraints. Removing the distance constraints from the WHAM protocol reproduced the Jarzynski-derived free energy.

We found that many discrepancies of SOD1 variants from WT were difficult to disentangle from the work profile but often emerged most naturally from the cumulative distribution of work values. Mechanical scans were thus used to construct the cumulative distributions, which then allowed us to distinguish the stabilizing energetics in various forms of PTM SOD1. In principle, different mechanical profiles could give rise to similar cumulative distributions, but in practice, this was never an issue. If cumulative distributions for two variants happened to be similar, their mechanical profiles could always be compared. Many of the properties we may be interested in for a given SOD1 variant involve coarse-grained properties of the protein that can be directly obtained from the cumulative distribution, such as how many residues are weakly stable given a threshold of work that perturbs the system.

By comparing the cumulative distribution of the work values for holo and metal-depleted SOD1 variants, we found that loss of either metal makes the protein more susceptible to structural deformation. Loss of Zn had a larger effect than loss of Cu. The loss of either metal modulated the entire mechanical profile, such that, by pairwise comparison, the work values no longer showed strong

correlation with those in the holo protein. The strongest correlation with holo protein was seen for (Cu-shift,E) SOD1, which lacks Zn and has Cu shifted to the Zn position ($r=0.32$, $p=0.03$). Interestingly, the work values of apo-SOD1 showed modest anticorrelation with those in holo-SOD1 ($r=0.37$, $p=0.01$), consistent with the idea that mechanically rigid residues in the holo protein are stabilized by the presence of metals and that mechanically rigid residues in the apo protein tend to be destabilized by the metals. This competition between apo state stability and metal-affinity-driven holo state stability was also seen in mutant studies, which revealed significant strain in the apo state.[5]

Our simulations showed that (Cu,E) SOD1 is substantially more mechanically malleable than (E, Zn) SOD1, which is consistent with previous experimental data: early work by Rotilio *et al.* found that the extent of recovery of the native copper site in terms of spectroscopic features and catalytic activity was related to the amount of residual zinc present,[54] implying that Zn aided the incorporation of Cu. Work from Lippard *et al.* later showed, by analyzing NMR shifts of coordinating histidine residues in the presence of a chemical modifier contingent on solvent exposure,[55] that Zn aided the incorporation of Cu by structuring the protein and that Zn alone was sufficient to structure the protein. Kayatekin *et al.* found substantial stabilizing free energies upon Zn binding, for all phases of structural organization of SOD1, dimeric to unfolded.[56]

Crystal structures of mutants that either inadequately or anomalously bind Zn show amyloid filament-like nonnative interactions, further supporting the critical structural role of Zn. Elam *et al.* find that the crystal structures of both apo-H46R and S134N, for which chain B has only one Zn ion bound in the Cu position, show similar and significant structural disorder in which nonnative contacts are made between the electrostatic loop from one domain and an exposed cleft made by β strands 5 and 6 of a neighboring domain.[36] Nordlund *et al.* find a similar effect for the H63S/H71S/H80S/D83S variant,[57] which cannot bind Zn in the putative binding site but instead binds Zn in the Cu binding site for about three-fourths of the molecules. Histidine 48 fails to ligate the Zn ion and instead swings outwards, leading to structural disorder in loop IV, which in turn destabilizes loop VII. This loop then interacts with edge β strands in neighboring molecules, analogously to the apo-H46R and S134N crystal structures.

Consistent with the observations that the role of Zn is structural while the role of Cu is enzymatic, we found that the affinity for Cu is reduced by ≈11.4 kJ/mol in the absence of Zn, while the affinity for Zn is reduced to a lesser degree by ≈5.9 kJ/mol in the absence of Cu. In the simulation protocol we employed, all structures were equilibrated before applying constraints between C^{α} atoms; thus, the structural deformations associated with loss of the partner metal prior to the affinity measurement were accounted for. As well, we also accounted for the effects due to re-equilibration of the protein structure in the final state of the protein after extraction of the metal, in calculating the net affinity. This relaxation effect is more significant for Zn than for Cu due to the stronger coupling of native structure to Zn binding and is most significant for dimer separation because of the removal of steric constraints and large change in interaction energies (see Figs. S3, S4, and S5). However, metal binding free energies were obtained from a metal expulsion process along "the most likely" pathway, but they did not consider all possible pathways of escape—the contribution of all other pathways is an entropy contribution that would likely result in modest reduction in the estimate for the binding free energy. Nevertheless, our measurements should give a good approximation to the relative differences in affinity between species. The decreased metal affinity of ALS-associated mutants points toward the general role of metal loss in the misfolding and propagation process.

Kayatekin *et al.* obtain larger values of Zn binding free energies of about 56 kJ/mol per monomer.[12] Although these values are obtained from several approximations, including the use of C6A/C111S and C6A/C111S/F50E/G51E as reference states for dimeric and monomeric WT SOD1, it is instructive to investigate reasons on the computational side as to why their value might be larger than our value of 40 kJ/mol. Our calculations obtain the binding free energy for monomeric SOD1 and, thus, neglect cooperativity effects between monomers in Zn binding to the dimer state. As well, although the OPLS-AA/L force field used in our simulations attempts to account for the electronic polarization of histidines that are critical in modulating metal binding free energies, polarization may still be underestimated by the force field. The discrepancy between our value of Cu binding free energy to WT SOD1 and that of Crow *et al.*[53] indicates that histidine polarization may be particularly important in Cu binding.

Further information on the loss of structure due to metal depletion is obtained from studies of the solution structure of the obligate monomer mutant E133Q/F50E/G51E, for which Banci *et al.*[13] found that the electrostatic and zinc-binding loops were severely disordered and extensively mobile in the absence of both metals but not in the absence of Cu alone, that is, for the (E,Zn) variant. Crystal structural studies of the apo WT protein also confirm that, for monomers devoid of metals, the electrostatic and Zn-binding loops are disordered and not visible in the electron density maps.[14] Some monomers in this study with 20% occupancy at the Zn site possessed well-ordered Zn-binding and electrostatic loop

regions; however, this was thought to be due to crystal packing forces. Roberts *et al*. have crystallized a constitutively Zn-deficient but Cu-containing SOD mutant H80S/D83S/C6A/C111S by mutating two zinc-binding ligands to hydrogen-bonding serines.[7] This variant was observed to have a disrupted dimer interface and partly disordered zinc binding and electrostatic loops. Both our mechanical pulling and simulation results are consistent with these observations (Table 2). In Fig. S7b and c, the increase in mechanical malleability and the magnitude of fluctuations upon metal release are measured for several regions SOD1, including residues 1–48, residues 48–83 constituting the Zn-binding loop, residues 84–120, residues 121–142 constituting the electrostatic loop, and residues 143–153. These plots show that loops IV and VII undergo systematic softening and increased fluctuations compared to other regions, as metals and in particular Zn are lost from the protein.

The mechanical response to the loss of metals that we observed was not localized to loops IV and VII and, in this sense, apparently differs from the above observations and constitutes a prediction of the model (Table 2). For example, while the mean mechanical stability of loops IV and VII decreased substantially after the loss of ZN or both metals, some regions of the protein such as β strands 3 and 6 are more rigid for the apo and (Cu,E) proteins than for the holo protein. Metal depletion of the WT enzyme modulated the entire mechanical stability profile, locally and nonlocally.

Our pulling simulations, which incur a significant perturbation on the structure, measure a quantity that is distinct from thermal fluctuations in the native ensemble. As such, they may show discrepancies with experimental probes measuring equilibrium fluctuations. Supporting this, the work values to extend to 5 Å do not correlate with the RMSD values for the corresponding residues (Table S3). As well, normal modes of the fluctuation spectrum for β sheets may involve, for example, sliding motions that are transverse to the radially directed pulling simulations that we employed. On the other hand, misfolding-related processes likely involve motions that are larger deformations beyond native basin fluctuations; thus, the information gained from relatively large mechanical perturbations can be useful in understanding misfolding.

We saw that PTMs, as well as ALS-associated mutations, reduced both metal affinity and dimer stability. This is consistent with experimental observations that mutations seemed to favor increased formation of Zn-free monomeric intermediates.[62] Several ALS-associated mutations that we investigated reduced holo dimer stability moreso than did disulfide reduction or loss of metals from the holo WT protein. On the other hand, apo(SH) WT SOD1 had lower dimer stability than 15/22 holo ALS-associated mutants; metal depletion along with disulfide reduction has larger consequence for monomerization than many mutations do alone. The apo mutants may have lower dimer stability still, however. The decrease in dimer stability of holo WT protein due to disulfide reduction, about 37 kJ/mol, is more significant than depletion of either metal, but not both (about 43 kJ/mol). The decrease in dimer stability due to Cu depletion is the smallest change of all modifications we investigated, about 12 kJ/mol, while the decrease in dimer stability due to Zn depletion is significant, about 28 kJ/mol. Increased concentrations of oxidatively modified monomeric species have been observed on pathway to aggregate formation by dynamic light-scattering measurements,[10] supporting the notion of monomers as an amyloid precursor. As well, aggregation rates have been observed to increase with decreased concentration of SOD1, which strongly indicates that monomeric species act as precursors to aggregation.[46] Small molecules targeted to stabilize the dimer interface have been observed to significantly inhibit *in vitro* aggregation in mutants A4V, G93A, and G85R.[63]

We found the dimer binding free energy of apo WT protein to be about 62 kJ/mol, which is in quite good agreement with experimental estimates derived from equilibrium denaturation data on C6A/C111A double mutants by extrapolating the destabilizing effects of the C6A/C111S double mutation ($\Delta G_{2M\rightarrow M_2} \approx 61\ kJ/mol$[51] ; see Table 2). Fits of equilibrium denaturation data of the pseudo-WT mutant protein C6A/C111S to three-state models give somewhat smaller numbers for dimer stability for the double mutant of about 51–52 kJ/mol.[48,51,60] Stroppolo *et al*. report a dimer stability for apo WT protein of about 52 kJ/mol[64]; however, these studies also predicted moderately smaller dimer affinity for the holo protein than the apo protein (about 49 kJ/mol), in contrast to our results.

The ALS-associated mutant S134N has been observed experimentally to have only moderate effects on thermodynamic stability,[12] indicating that mechanisms aside from global unfolding play a role in disease propagation. Indeed, we observe significant effects on both metal affinity and dimer stability for this variant: the dimer stability is reduced from the WT by 45 kJ/mol, and the Zn binding free energy is reduced from the WT by 12 kJ/mol. Kayatekin *et al*. also see a Zn binding free energy for an obligate monomeric form of this mutant (C6A/C111S/F50E/G51E/S134N) that is reduced from the C6A/C11S/F50E/F51E form by 7 kJ/mol, based on the ratio of their K_d values.[12] On the other hand, some of their obligate monomeric mutants have higher free energy for Zn binding (e.g., their $\Delta\Delta G$ values for A4V, G93A, L38V, and S134N are −2.9, −1.7, +2.9, and +6.7 kJ/mol, respectively). This contrasts with

the consistent decrease in Zn affinity for ALS mutants that we have seen here and may be due to the mutations present in their pseudo-WT background. That said, our values of $\Delta\Delta G$ for Zn binding free energy correlate very well with theirs (see Table S1): $r=0.99$, $P_V=0.01$. Consistent with Crow *et al*., we do see reduced metal affinity for all fALS mutants considered[53]; however, our values for Zn binding free energy did not correlate with their values (of A4V, L38V, and I113T), possibly due to monomerization during the course of the affinity measurements.[12] Our values for Cu binding free energy did correlate with their values ($r=0.78$); however, the number of mutants (3) is not enough to be statistically significant.

The binding free energy of Zn to WT SOD1 monomer as measured experimentally by Khare *et al*. is about 40 kJ/mol,[46] which is in excellent agreement with our value of 40 kJ/mol. However, their value was obtained at pH 3.5, which would reduce the value from that at pH 7. Likewise, calorimetry measurements at pH 5.5 by Potter *et al*. give comparable numbers of at least 45 kJ/mol for binding the first Zn ion to apo-SOD1 homodimer.[52] In Ref. 46, the authors also observed that metal depletion, facilitated by dialysis against metal-free buffer, promoted aggregation at 30 μM and pH 3.6. We cannot address whether metal depletion occurs before or after monomerization along the aggregation pathway, and this does not appear to be a settled issue. As well, the total free-energy change from holo dimer to a monomerized (Cu,E) form is independent of the sequence in which these changes occur; thus, in principle, both parallel pathways may be undertaken and would give the same net result, provided that this part of the misfolding/aggregation reaction is under thermodynamic control.

Our calculations for dimer stability have 14 fALS mutants in common with the calculations of Khare *et al*.[65]; however, we see no correlation between our apo dimer stability values for these mutants (Table S1) and their values for either the free energy of dissociation of the dimer or the overall thermodynamic stability of the dimer ($r=0.001$ and $r=0.08$). These authors mention that one possible source of discrepancy between their values and experimentally determined stabilities is that their simulations relied on the assumption that there is no major structural change in the protein upon mutation. Their values also rely on calculations of absolute free energies,[66,67] for which it is often challenging to obtain quantitative accuracy, in contrast to relative changes in the free energy. We have sought to be careful here in calculating relative changes in free energy, including relaxation after mutation or PTM by thermal equilibration, and also re-equilibration in the final state after dimerization or metal extraction. Relaxation free energies in demetallation generally vary mutant to mutant and were more substantial for re-equilibration of disulfide-reduced or Zn-depleted SOD1 (Figs. S3 and S4). Relaxation free energies for monomerization were larger than for demetallation and were most significant for apo(SH) SOD1, followed by apo(SS) and (Cu,E) SOD1 (Fig. S5). These variants had significantly increased entropy in the monomeric state from the dimeric state because of the loss of dimer interface constraints on the zinc-binding loop.

Rumfeldt *et al*. have found that, for fALS mutants E100G, G93A, and G85R inserted into the pseudo-WT background C6A/C111S, dimer stability was largely unaffected by mutation.[47] In contrast, we found significant weakening of dimer stability due to the mutant G85R, albeit in the pure WT background of holo protein. Similar investigations from Vassall *et al*. have shown that the same mutations in the apo dimer did weaken dimer stability; however, the decreases in dimer stability that we have calculated are substantially larger than their values.[48] These difference may be reconciled by computational studies of the binding free energy for fALS mutants with explicit pseudo-WT backgrounds (e.g., triple mutants here); mutation of the cysteines may modulate the dimer stability and alter free energetic differences between mutants and WT. Experimental evidence suggests, however, that these effects may be modest[51,68]; however, the computational study is an interesting topic for future work.

Several previous studies, including those of Lindberg *et al*.,[51] Arnesano *et al*.,[8] and Doucette *et al*.,[69] have found that, for pseudo-WT SOD, either Zn binding or formation of the C57–C146 disulfide bond was sufficient to induce or rescue dimer formation, that is, both the absence of metals (apo) and reduction or ablation of the disulfide bond are necessary to induce monomer formation, even at low concentrations (~10 M SOD1). Sedimentation velocity analysis[69] indicates that both holo-C57S and apo-SOD1 sediment as dimers, with apo-SOD1 marginally more monomer-like. Consistent with these observations, we found that both metal depletion and disulfide reduction had significant destabilizing effects on dimer stability. The holo(SH) dimer had lower binding free energy than that for either the (Cu,E) or (E,Zn) variants, but the apo dimer had lower dimer binding free energy than the holo(SH) dimer; this result that binding of both metals (holo *versus* apo) plays a larger role than disulfide formation in dimer affinity is consistent with simulations from Ding and Dokholyan, based on interdomain native contact data.[70] Demetallation destabilized the disulfide-reduced dimer by about 7 kJ/mol. However, we found that disulfide reduction only further destabilized the apo dimer by about 1 kJ/mol, in apparent contrast to the observation that apo(SS) SOD1 elutes as a dimer but apo(SH) SOD1 elutes as a monomer. One possible resolution here is the role that increased entropy might play in the

reduced protein in rebinding a partially disrupted interface. Further work will be required on the computational side to reconcile these observations.

The mutants H46R, H46R/H48Q, and D125H were atypical in that the Zn affinity was larger than the Cu affinity (though only marginally for D125H). The first two of these variants have mutations in Cu-coordinating residues; thus, the reversal in affinity was not surprising. For D125H, the reasons are more subtle however. The center of mass of the aspartic acid side chain is 12 Å from the Cu and 11 Å from the Zn, respectively; thus, the coupling to binding free energy involves bridging interactions through at least two side chains. This system provides another example of nonlocal communication in the protein through stress–strain networks.

Cu^{1+} affinity is quite modest for mutants, indicating ready release of monovalent Cu in the reduced phase of the catalytic cycle. Released or exposed Cu is capable of reacting nonspecifically with a variety of substrates to produce reactive oxygen and nitrogen species that are toxic to intracellular structures, including microtubules, metabolic enzymes, and signaling proteins.[71] Reactive species may oxidatively modify side chains to inactivate SOD1[72] and induce its misfolding[27]; positive feedback loops have been identified between protein misfolding and excitotoxicity.[73]

By simulating AFM-like probes, we investigated the mechanical stability of holo, holo(SH), apo, and apo(SH) variants of WT protein. Here we found that the apo variant was less mechanically stable than holo(SH) (statistical significance $p \approx 3 \times 10^{-8}$), indicating that metal depletion is more mechanically destabilizing than disulfide reduction. This is consistent with differential scanning calorimetry (DSC) measurements of the melting temperatures of SOD1 variants, where (E,Zn)(SH) SOD1 was observed to have larger T_m than the apo variant by about 9 °C.[58] Similarly, Cu,E(SS) is more mechanically stable than holo(SH) SOD1 (Fig. S6), and we anticipate that DSC and other measurements of this system would recapitulate the results of apo(SS) and holo(SH) (Table 2). Intriguingly, we found that apo(SH) monomer was more mechanically stable than apo monomer ($p \approx 8 \times 10^{-8}$). This observation was supported by time-resolved simulations of the relaxation kinetics of the internal potential energy. These showed that the protein internal potential energy increased upon disulfide reduction for the holo protein, indicating decreased stability through loss of stabilizing interactions. However, the protein internal potential energy decreased upon disulfide reduction for the apo protein, indicating *increased* stability and relaxation of frustrating interactions. The existence of frustration in the apo state is supported by analysis of the mechanical stability of C-terminal truncation mutants, native basin dynamic fluctuation analysis, and frustration/potential energy analysis.[5] The potential energy increase after SS reduction in the holo protein indicates that entropy increase plays a role in the lowering of the free energy after the removal of constraints. The potential energy decrease after SS reduction in the apo protein indicates that the release of native stress upon removal of constraints is sufficiently large to be observed amidst the concomitant effects arising from entropy increase.

These results, at first sight, contrast with DSC measurements indicating that melting temperatures are larger for WT apo-SOD1 than for apo(SH) SOD1 by about 7 °C,[58] that is, the disulfide bond thermodynamically stabilizes the apo monomer. One important difference between the simulation probes and experimental measurements is that our mechanical probes measure stiffness in the native basin but not the relative difference in the free energies between the folded and unfolded states. While these generally correlate for one variant at different temperatures, they need not correlate for different protein variants at the same temperature, in particular, if one variant has larger entropy in the unfolded state, as is the case here because of the presence or absence of a disulfide constraint. It is possible to observe a stiffer native basin for a less thermostable protein, as indicated schematically in inset (c) of Fig. 6.

Zinc removal dominates the effects of metal depletion on mechanical stability. In fact, depletion of both metals results in lower mechanical stability than (Cu,E) SOD1 only for a few (~8) of the least stable residues [i.e., the statistical significance that the cumulative distribution of apo is weaker than (Cu, E) is about $p \approx 9 \times 10^{-3}$].

Insertion of metals into apo(SH) SOD1 indeed makes some regions very mechanically stable, increasing the stability of the most stable regions of the protein. However, the general trend over most of the residues is to mechanically destabilize the protein due to added internal stresses. Thus, metal depletion modestly stabilizes the disulfide-reduced protein mechanically ($p \approx 8 \times 10^{-3}$). Together with the observation that disulfide reduction mechanically stabilizes apo-SOD1, this evidence points toward cooperativity between metal binding and disulfide formation (Table 2). As mentioned above, mechanical stability need not be equivalent with thermodynamic stability: thermodynamic stability accounts for the free energy of the unfolded state, while our mechanical stability measurements do not.

For the Zinc-depleted form, shifting of the Cu to the Zn position resulted in a more robust mechanical stability profile ($p \approx 1 \times 10^{-7}$). Supporting this trend in stability, WHAM simulations of the transfer of Cu from the putative Cu binding site to the Zn binding site for the (Cu,E) form of the protein lowered the free energy by approximately −6 kJ/mol, indicating that the Zn binding position is more favorable for the Cu

when only Cu is bound. This provides further evidence that binding of Cu is under kinetic control, modulated essentially by the initial Zn-coordinated folding of the protein and its subsequent binding to the co-expressed Cu chaperone CCS, which selectively loads Cu to its putative site.[74] Computing the transfer free energy for Zn from the Zn-binding site to the Cu-binding site gives approximately +6 kJ/mol, supporting the model that Zn binding is thermodynamically controlled. Kinetics experiments by Leinartaite *et al*. indicate that Zn^{2+} binds to the putative Cu site during folding but may be transferred to the higher affinity Zn-binding site late in the folding process.[75] We note that the above transfer free energies are estimates and do not take into account the differential affinity due to the $3d^{10}$ *versus* $3d^{9}$ electronic valence of Zn^{2+} and Cu^{2+}, respectively.

The decrease in free energy corresponding to the shift of the Cu is accompanied by increased mechanical rigidity in the Zn-binding loop. However, some residues, such as residues 24, 75, and 120, are significantly weakened by the shift. Consistent with significantly weakened mechanical rigidity, the root-mean-square fluctuation values are increased for those residues, corresponding to an increase in local entropy. Similar effects were seen here for processes such as metal binding and disulfide formation—energetically favorable processes that result in local enhancement of structure but that may increase entropy nonlocally. Nonlocal entropy generation has also been seen in pulling simulations, where local mechanical stress induced by pulling on a particular residue resulted in nonlocal unwinding of the short stretches of α helix in the Zn-binding and electrostatic loops.[5]

These effects perhaps foreshadow one of the essential features of disease propagation in template-directed misfolding, namely, that of nonlocal entropy transduction across the protein. It is feasible that the induced misfolding of a protein due to the interaction with misfolded template would correspond to low enthalpy and low entropy in the vicinity of the binding interface, as well as high enthalpy and high entropy away from the binding interface. Such a phenomenon would facilitate the structural plasticity required to render the protein amenable to adopt altered conformations in the presence of misfolded template. Once altered conformations are adopted, the misfolded protein becomes part of the infectious species, capable of further seeding misfolding through the reservoir of healthy protein.

Methods

Steered molecular dynamics simulations

Steered molecular dynamics with constant-velocity moving restraints involving two tethering points was used to simulate the action of a moving AFM cantilever on a protein. Three computational assays were investigated:

1. A study of SOD1 monomer, where one tether was placed at the position of the C^{α} closest to the center of mass of the protein [generally $C^{\alpha}(46)$], and another tether was placed on the C^{α} of a particular amino acid to be pulled on.
2. A study of monomerization from the dimer, with a tether on the C^{α} atom closest to center of mass of each monomer.
3. A study of metal removal, with one tether on the C^{α} atom of either residue Phe45 (for Cu removal) or that of Asp83 (for Zn removal) and the other tether on either the Cu or Zn metal ion. These residues are chosen because they determine the approximate direction of highest solvent exposure of the metal.

In assay (1), to implement a mechanical stability scan across the surface of the protein, we selected every fifth amino acid along with the first and last residues for a pulling simulation. This coarse-grains the mechanical profile so that the work values obtained are a sampling of the work values for all residues.

As described in Ref. 5, steered molecular dynamics simulations[76–79] were preformed in GROMACS using an all-atom representation of the protein, with OPLS-AA/L parameters[80,81] and a generalized Born surface area implicit solvent model with protein dielectric constant of 4, solvent dielectric constant of 80, and surface tension coefficient for solvation free energies of 0.005 kcal/mol/Å^2.[82] Born radii are calculated from the Onufriev–Bashford–Case algorithm,[83] and bond lengths containing a hydrogen atom are constrained by the LINCS algorithm.[84] The long-distance cutoff used for nonbonded interactions was 14 Å for both electrostatic and van der Waals interactions.

After energy minimization by steepest descent to remove potential steric clashes, simulations were implemented using an integration timestep of 2 fs, in a cubic simulation box with periodic boundary conditions and size such that all protein atoms were initially at least 20 Å from any cubic face. An equilibrium simulation was always run for 20 ns to equilibrate the protein before any pulling simulations were performed and data were collected; coordinates were saved every 100 ps.

Because only moderate deformations were required to construct mechanical force-extension curves, a very slow pulling speed (for simulations) of 2.5×10^{-3} m/s was admissible when work values were computed. This speed is 400–8000× slower than the speeds generally used in simulations[85–87] and is comparable to pulling speeds used in AFM experiments.[88] The spring constant of the simulated AFM cantilever was taken to be 5 kJ/mol/Å^2, which is comparable to the protein effective spring constant.

For assay (1), each pulling simulation ran until the change in distance between the two tethering points was 5 Å. For assays (2) and (3), the simulations were continued until the force fell to a value of zero indicating the separation of the dimer or demetallation of the monomer, respectively.

Tethering residues

The C^{α} atom of residue 46 was closest to the center of mass for WT SOD1 and all variants. For mechanical

scans, residues 40, 45, 50, 54, and 55 were either too close to the central C^{α} or along the same β strand and gave anomalous force-extension profiles with artificially large forces probing covalent bonding topology moreso than noncovalent stabilizing interactions. In these cases, the tethering residue was moved to residue 76. This always resolved the problem of large forces. In assay (2) for dimer pulling simulations, the tethering point (on each of the monomers) was $C^{\alpha}(46)$.

In assay (3) for Cu and Zn pulling simulations, the tethering point was $C^{\alpha}(45)$ for Cu extraction and $C^{\alpha}(83)$ for Zn. The residue selection was chosen by finding residues within 5 Å of the metal and by selecting the residue that was the most buried (least solvent-accessible surface area) as the tethering residue. The resulting pathways are shown in the insets of Fig. 3a. For the analysis of the (Cu,E) variant PDB 2R27, the Cu ion of chain A was shifted by 1.3 Å to a location associated with reduced (Cu^{1+}) that is closer to the putative Zn position. For this protein, the tethering residue was taken to be $C^{\alpha}(83)$.

Residues used for mechanical scans of protein stability

Every fifth residue along the protein sequence, including the first and the last residues, was taken as a tethering residue. As well, the central positions of the predicted epitopes and anti-epitopes were added to the data set,[89] as described in Ref. 5. If the center of the epitope happened to coincide with a multiple of 5 already included in the scan (e.g., residue 10), then the next residue (residue 11 in this case) was also taken. Thus, a set of 48 residues was used in the mechanical scans: 1, 5, 10, 11, 15, 17, 20, 24, 25, 30, 31, 35, 38, 40, 45, 46, 50, 54, 55, 60, 65, 70, 73, 75, 80, 85, 90, 91, 95, 100, 101, 105, 108, 110, 115, 120, 121, 125, 130, 135, 136, 140, 141, 145, 146, 150, 151, and 153.

Proteins considered

Proteins whose mechanical profiles were calculated are given in Table 1. For (Cu,E) SOD1, 2R27 was used to generate an initial structure with the Cu shifted to the Zn position (as it exists in the PDB structure) and a (Cu,E) variant with the Cu in its putative position, by moving the Cu and equilibrating the structure.

Several mutants were also considered for the calculation of metal affinity and dimer affinity. These included A4V, D124V, D125H, D76Y, D90A, G127X, G37R, G41D, G41S, G85R, G93A, G93C, H43R, H46R, H46R/H48Q, H80R, I113T, L144F, L38V, S134N, T54R, and W32S. The corresponding PDB entries used to generate structures for these mutants for simulations are given in Table 1.

Remodeling disordered/missing regions in PDB structures

(Cu,E) SOD1 (2R27) has two unstructured segments in the crystal structure, residues 68–78 and residues 132–139; however, a full-length construct must be used as an initial condition in simulations. The missing segments were added to the protein by the following method: first, segments of protein corresponding to the missing sequences were taken from the native holo-SOD1 structure, and replica exchange molecular dynamics simulations of the free peptides in explicit solvent[90] were performed using the NAMD simulation package,[91] to obtain an ensemble of disordered conformations for these two peptide fragments. Clustering was then performed on the simulated ensemble for each peptide,[92] and a conformation was chosen from the largest cluster, such that its end-to-end distance best matched the corresponding distance between the structured residues present in 2R27 that bracketed the missing sequence. After adding the missing loop segments, we "back-mutated" four residues, A6C, S80H, S83D, and S111C, to recover the WT sequence, using the PyMOL software package.[93] The structure was then energy minimized and equilibrated for 20 ns, as described in Steered molecular dynamics simulations. A full-length construct was thus assembled to be used as an initial condition in pulling simulations.

Modeling proteins with no PDB structure

Some proteins studied here had no PDB structural coordinates available (see Table 1). For these proteins, a structure was built by modifying known PDB structures of similar proteins. For example, disulfide-reduced WT SOD1 was created from (E,Zn)(SH) SOD1 (2AF2) by adding Cu to that structure and back-mutating A6C and S111C using the PyMOL software package.[93] Apo WT SOD1 was created from the apo-SOD1 structure PDB 1RK7 by back-mutating Q133E, E50F, and E51G. Apo(SH) SOD1 was created from the apo WT SOD1 structure 1RK7 by reducing the disulfide linkage and mutating E50F, E51G, and Q133E. The mutant H46R was generated from the H46R/H48Q double mutant of SOD1 by back-mutating Q48H. Similarly, the mutants W32S, G41S, G41D, G93C, L144F, D90A, and D76Y were prepared from the holo-SOD1 by mutating at the respective positions. The G127X mutant was created from holo-SOD1 by deleting the last 20 residues and then mutating the last 6 residues of the remaining sequence (KGGNEE) to correspond to the frame-shifted nonnative C-terminal peptide sequence (GGQRWK) prior to the termination sequence. All modified structures were energy minimized and equilibrated for 20 ns by running an equilibrium simulation, before performing any pulling assays.

Umbrella sampling and WHAM

WHAM procedure for mechanical profiles

Initial configurations for use in WHAM were obtained from the pulling simulations described in Steered molecular dynamics simulations: 25 initial conditions between 0 and 5 Å were simulated for 10 ns each, in an umbrella potential with stiffness 500 kJ/mol/nm^2 to constrain the simulations near their corresponding separation distances. These 25 simulations are then used to reconstruct the free-energy profile along the distance coordinate using the WHAM,[94] and the free-energy difference between 0 and 5 Å is then obtained.

A convergence check assured that the result was unchanged if 30, 35, or 40 windows were used.

WHAM procedure for metal expulsion and dimer separation

To obtain free energies of metal binding, we inserted metals into the putative binding locations for all SOD1 variants, where they were found to be at least metastable. Dimer stabilities were calculated under the same metallation conditions as the PDB structure for all mutants. Mutants with no structure in the PDB were fully metallated.

For the metal expulsion free-energy calculations in ALS-associated SOD1 mutants show decreased affinity for both Cu and Zn, a most direct straight-line path was first determined for the pulling direction as described in Steered molecular dynamics simulations, which determined the tethering residue. The metal was pulled away from the protein using a spring constant of 500 kJ/mol/nm^2 and a pull rate of 0.01 nm/ps. For purposes of the free-energy calculation, the final extension from the equilibrium distance between metal and tethering residue was taken to be approximately 30 Å. From these trajectories, snapshots were taken to generate the starting configurations for the umbrella sampling windows.[95–97] An asymmetric distribution of sampling windows was used, such that the window spacing was 1 Å between 0 and 20 Å of separation and was 2 Å beyond 20 Å of separation. Such spacing allowed for increasing detail at smaller separation distances and resulted in a total of 25 windows. In each window, 10 ns of molecular dynamics was performed for a total simulation time of 250 ns utilized for umbrella sampling. Analysis of the results was performed using the WHAM.[94]

To remove conformational distortion effects on the free energy, we applied position restraints in the following way. For a given C^α atom in the protein, all other C^α atoms within 5 Å were constrained to have a roughly constant C^α–C^α distance, the same as in the equilibrated structure, using spring constants of 392×10^3 kJ/mol/nm^2. The spring constant was varied to interpolate between regimes where protein deformation is dominant and a regime where the constraining C^α–C^α network can potentially influence the expulsion free energy. Using C^α constraints allows the protein to retain its structure under force while still allowing the side chains and partially the backbone to fluctuate in response to the external perturbation. After metal expulsion, C^α constraints were relaxed and the relaxation free energy was calculated as described below.

A similar procedure was employed for dimer separation. Here the tethering points were taken to be the C^α atom of residue 46 in each of the monomers. The monomers constituting the dimer were pulled away from each other, until the final distance was approximately 30 Å. The spring constant, pull rate, and window separation were the same as in the metal expulsion analysis. Within each monomer, C^α constraints were also applied to fix the relative positions of the C^α atoms near their equilibrium positions and thus minimize conformational distortion during monomerization.

The free energy for metal expulsion or dimer separation was corrected to account for protein relaxation in the final metal-depleted or monomerized state: $\Delta F_{\text{tot}}=\Delta F_{\text{constr}}+\Delta F_{\text{relax}}$. That is, after either metal expulsion or monomerization, C^α constraints are gradually reduced from 392×10^3 kJ/mol/nm^2 to 0 using 30 windows and 10 ns of relaxation time in each window, and free-energy changes for this process are again obtained using WHAM. Convergence of the free-energy values was tested by both varying the number of windows (to 30, 35, and 45) and varying the length of the equilibrium simulation in each window (to 15, 20, 25, and 30 ns). In all cases, the free energies were seen to have converged using the original protocol.

To further confirm that equilibrium has been reached, we constructed thermodynamic cycles for either re-insertion of the metal or re-dimerization of the monomers. The metal or dimer binding free energies subject to C^α constraints were calculated, as well as the subsequent relaxation free energies. Schematics of the thermodynamic cycles are plotted in Fig. 4, and values of each of the free-energy changes for WT protein and several mutants are given in Table S2.

WHAM procedure for shifting Cu to the Zn binding position

In the simulated conformations of (Cu,E) SOD1 that have been equilibrated from the crystal structure 2R27 (in which Cu is bound close to the putative Zn position), Cu remains close to the Zn position and does not shift back to the Cu binding site. The distance between the position of the Cu ion in the equilibrated structures from simulations of holo WT SOD1 and the above (Cu,E) SOD1 is 7.92 Å. We calculated the free-energy change to move Cu from its putative binding position to the Zn position with the following method. We first pulled the Cu from its original position to the (Zn binding) equilibrated position by applying a spring constant of 500 kJ/mol/nm^2 and a pulling speed of 10 m/s while enforcing harmonic constraints on all of the C^α atoms as in WHAM procedure for metal expulsion and dimer separation. Tethers were placed on the Cu ion and the C^α atom of residue 57 because it is almost on the line joining the initial and final positions of the Cu. Conformations were collected after every 0.5 Å, and for each of the conformations, a 10-ns molecular dynamics simulation was performed. These trajectories were used for umbrella sampling, and analysis of the results was performed using WHAM.

Free-energy differences from Jarzynski equalities and finite sample-size corrections

The free-energy cost ΔF to extend a residue to 5 Å is found from Jarzynski's equality

$$\Delta F = -kT \ln\left\langle e^{-W/kT}\right\rangle \tag{1}$$

where W is the work from a non-equilibrium measurement, kT is Boltzmann's constant times the temperature in Kelvin, and the average $\langle\cdots\rangle$ is the ensemble average over replicated pulling assays. For a finite sample size, the free energy in Eq. (1) becomes

$$\Delta F_J = -kT \ln\left\langle e^{-W/kT}\right\rangle_N = -kT \ln\left(\frac{1}{N}\sum_{i=1}^{N} e^{-W/kT}\right) \tag{2}$$

which must be corrected because of systematic bias for finite sample size. Following Gore *et al.*, an estimate for the

free-energy change ΔF that accounts for finite sample-size corrections is given by the following set of equations[42]:

$$\Delta F = \Delta F_J - \frac{\overline{W}_{dis2}}{N^{\alpha}(\overline{W}_{dis2})} \quad (3)$$

$$\overline{W}_{dis2} = \overline{W}_{dis2} + \frac{\overline{W}_{dis2}}{N^{\alpha}(\overline{W}_{dis})}$$

$$\overline{W}_{dis} = \langle W \rangle_N - \Delta F_J$$

$$\alpha(W) = \ln(2W/kT) / \ln\left[C\left(e^{2W/kT} - 1\right)\right]$$

In the above equations, $\langle W \rangle_N$ is the average work for the N pulling assays, and $\overline{W}_{dis}$ is the average dissipated work—work that did not go into producing the free-energy change. The function $\alpha(W)$ is evaluated at two values of dissipated work, $\overline{W}_{dis}$, and a corrected estimate for the dissipated work, $\overline{W}_{dis2}$, which accounts for the fact that $\overline{W}_{dis}$ is itself an underestimate because of the finite sample-size bias. The constant appearing in $\alpha(W)$ defines a crossover between small N and large N regimes and is not rigorously determined. We take $C = 15$ following Gore *et al.*[42]

Table S6 gives numerical values for the various quantities in Eq. (3), in the assay where residues 10 and 17 are pulled to 5 Å. The mean dissipated work $\overline{W}_{dis2}$ in our pulling assay is only about 1 kJ/mol, indicating that pulling is near equilibrium and finite sample-size corrections are not large, about 1–3 kJ/mol.

Statistical analysis

To compare whether the difference between two distinct cumulative distributions is statistically significant, we use the method described in Ref. 5. A summary of the method follows. The mechanical profile is a collection of 48 work values for a given SOD1 variant, where each work value has an error of $\sigma = 2.7$ kJ/mol. We wish to answer the following question: given one work profile and its resultant cumulative distribution, along with the error bars associated with the individual work values, what is the probability of obtaining cumulative distributions at least as extreme as another given one by chance, that is, as arising from the original work profile?

To find the above probability and thus determine the statistical significance of a given cumulative distribution, we employ a "Monte Carlo" procedure of generating cumulative distributions from a given "baseline" work profile. For example, to test the hypothesis that shifting the Cu from its putative position to the Zn binding position mechanically stabilizes the (Cu,E) protein, we wish to find the probability of obtaining a cumulative distribution at least as stabilized as the (Cu-shift,E) cumulative distribution from the original (Cu,E) cumulative distribution. The (Cu-shift,E) cumulative distribution has 31 work values that are more stable than those in the (Cu,E) cumulative distribution; the difference in work values is plotted in Fig. S2c, largest to smallest. We seek cumulative distributions that have rank-ordered deviations at least as large as those of the (Cu-shift,E) cumulative distribution. Work profiles are constructed by adding Gaussian noise of mean zero and standard deviation $\sigma = 2.7$ kJ/mol to the baseline work profile [here, that of (Cu,E) SOD1]. A cumulative distribution is then constructed for each generated profile by sorting the values lowest to highest. After constructing N of such cumulative distributions, we ask whether one has found a cumulative distribution with, for example, rank-ordered positive deviations at least as large as those in the (Cu-shift,E) cumulative distribution. The value of N where the expected number of trajectories is unity determines the statistical significance of the difference between the two profiles: $p = 1/N$. Plots of the corresponding distributions for (Cu,E) SOD1 and (Cu-shift,E) SOD1 are given in Fig. S2.

Acknowledgements

We thank Neil Cashman, Will Guest, Stephen Toope, Paul Whitford, and Michael Woodside for helpful and/or supportive discussions. We also acknowledge funding from PrioNet Canada and acknowledge computational support from the WestGrid high-performance computing consortium.

Supplementary Data

Supplementary data to this article can be found online at http://dx.doi.org/10.1016/j.jmb.2012.12.022

Received 11 July 2012;
Received in revised form 8 November 2012;
Accepted 21 December 2012
Available online 3 January 2013

Keywords:
superoxide dismutase;
ALS;
molecular dynamics simulations;
thermodynamic stability;
protein misfolding

† http://alsod.iop.kcl.ac.uk/

Abbreviations used:
ALS, amyotrophic lateral sclerosis; PTM, post-translational modification; WT, wild type; WHAM, weighted histogram analysis method; PDB, Protein Data Bank; DSC, differential scanning calorimetry.

References

1. Tainer, J. A., Getzoff, E. D., Beem, K. M., Richardson, J. S. & Richardson, D. C. (1982). Determination and analysis of the 2 Å structure of copper, zinc superoxide dismutase. *J. Mol. Biol.* **160**, 181–217.
2. Bertini, I., Manganl, S. & Viezzoli, M. S. (1998). Structure and properties of copper-zinc superoxide dismutases. *Adv. Inorg. Chem.* **45**, 127–250.

3. Valentine, J. S., Doucette, P. A. & Zittin Potter, S. (2005). Copper-zinc superoxide dismutase and amyotrophic lateral sclerosis. *Annu. Rev. Biochem.* **74**, 563–593.
4. Shaw, B. F. & Valentine, J. S. (2007). How do ALS-associated mutations in superoxide dismutase 1 promote aggregation of the protein? *Trends Biochem. Sci.* **32**, 78–85.
5. Das, A. & Plotkin, S. S. SOD1 exhibits allosteric frustration to facilitate metal binding affinity, *Proc. Natl Acad. Sci. USA* (Revised manuscript submitted).
6. Getzoff, E. D., Cabelli, D. E., Fisher, C. L., Parge, H. E., Viezzoli, M. S., Banci, L. & Hallewell, R. A. (1992). Faster superoxide dismutase mutants designed by enhancing electrostatic guidance. *Nature*, **358**, 347–351.
7. Roberts, B. R., Tainer, J. A., Getzoff, E. D., Malencik, D. A., Anderson, S. R., Bomben, V. C. *et al.* (2007). Structural characterization of zinc-deficient human superoxide dismutase and implications for ALS. *J. Mol. Biol.* **373**, 877–890.
8. Arnesano, F., Banci, L., Bertini, I., Martinelli, M., Furukawa, Y. & O'Halloran, T. V. (2004). The unusually stable quaternary structure of human Cu, Zn-superoxide dismutase 1 is controlled by both metal occupancy and disulfide status. *J. Biol. Chem.* **279**, 47998–48003.
9. Hough, M. A., Grossmann, J. G., Antonyuk, S. V., Strange, R. W., Doucette, P. A., Rodriguez, J. A. *et al.* (2004). Dimer destabilization in superoxide dismutase may result in disease-causing properties: structures of motor neuron disease mutants. *Proc. Natl Acad. Sci. USA*, **101**, 5976–5981.
10. Rakhit, R., Crow, J. P., Lepock, J. R., Kondejewski, L. H., Cashman, N. R. & Chakrabartty, A. (2004). Monomeric Cu, Zn-superoxide dismutase is a common misfolding intermediate in the oxidation models of sporadic and familial amyotrophic lateral sclerosis. *J. Biol. Chem.* **279**, 15499–15504.
11. Hörnberg, A., Logan, D. T., Marklund, S. A. & Oliveberg, M. (2007). The coupling between disulphide status, metallation and dimer interface strength in Cu/Zn superoxide dismutase. *J. Mol. Biol.* **365**, 333–342.
12. Kayatekin, C., Zitzewitz, J. A. & Matthews, C. R. (2010). Disulphide-reduced ALS variants of Cu, Zn superoxide dismutase exhibit increased populations of unfolded species. *J. Mol. Biol.* **398**, 320–331.
13. Banci, L., Bertini, I., Cramaro, F., Del Conte, R. & Viezzoli, M. S. (2003). Solution structure of apo Cu, Zn superoxide dismutase: role of metal ions in protein folding. *Biochemistry*, **42**, 9543–9553.
14. Strange, R. W., Antonyuk, S., Hough, M. A., Doucette, P. A., Rodriguez, J. A., Hart, P. J. *et al.* (2003). The structure of holo and metal-deficient wild-type human Cu, Zn superoxide dismutase and its relevance to familial amyotrophic lateral sclerosis. *J. Mol. Biol.* **328**, 877–891.
15. Rosen, D. R., Siddique, T., Patterson, D., Figlewicz, D. A., Sapp, P., Hentati, A. *et al.* (1993). Mutations in Cu/Zn superoxide dismutase gene are associated with familial amyotrophic lateral sclerosis. *Nature*, **362**, 59–62.
16. Reaume, A. G., Elliott, J. L., Hoffman, E. K., Kowall, N. W., Ferrante, R. J., Siwek, D. R. *et al.* (1996). Motor neurons in Cu/Zn superoxide dismutase-deficient mice develop normally but exhibit enhanced cell death after axonal injury. *Nat. Genet.* **13**, 43–47.
17. Cleveland, D. W. & Rothstein, J. D. (2001). From Charcot to Lou Gehrig: deciphering selective motor neuron death in ALS. *Nat. Rev., Neurol.* **2**, 806–819.
18. Hart, P. J. (2006). Pathogenic superoxide dismutase structure, folding, aggregation and turnover. *Curr. Opin. Chem. Biol.* **10**, 131–138.
19. Rakhit, R. & Chakrabartty, A. (2006). Structure, folding, and misfolding of Cu, Zn superoxide dismutase in amyotrophic lateral sclerosis. *Biochim. Biophys. Acta*, **1762**, 1025–1037.
20. Gaudette, M., Hirano, M. & Siddique, T. (2000). Current status of SOD1 mutations in familial amyotrophic lateral sclerosis. *Amyotroph. Lateral Scler. Other Motor Neuron Disord.* **1**, 83–89.
21. Shibata, N., Hirano, A., Kobayashi, M., Sasaki, S., Takeo, K., Matsumoto, S. *et al.* (1994). CuZn superoxide dismutase-like immunoreactivity in Lewy body-like inclusions of sporadic amyotrophic lateral sclerosis. *Neurosci. Lett.* **179**, 149–152.
22. Bosco, D. A., Morfini, G., Karabacak, N. M., Song, Y., Gros-Louis, F., Pasinelli, P. *et al.* (2010). Wild-type and mutant SOD1 share an aberrant conformation and a common pathogenic pathway in ALS. *Nat. Neurosci.* **13**, 1396–1403.
23. Forsberg, K., Jonsson, P. A., Andersen, P. M., Bergemalm, D., Graffmo, K. S., Hultdin, M. *et al.* (2010). Novel antibodies reveal inclusions containing non-native SOD1 in sporadic ALS patients. *PLoS One*, **5**, e11552.
24. Furukawa, Y., Kaneko, K., Yamanaka, K. & Nukina, N. (2010). Mutation-dependent polymorphism of Cu, Zn-superoxide dismutase aggregates in the familial form of amyotrophic lateral sclerosis. *J. Biol. Chem.* **285**, 22221–22231.
25. Ding, F., Furukawa, Y., Nukina, N. & Dokholyan, N. V. (2012). Local unfolding of Cu, Zn superoxide dismutase monomer determines the morphology of fibrillar aggregates. *J. Mol. Biol.* **421**, 548–560.
26. Estévez, A. G., Crow, J. P., Sampson, J. B., Reiter, C., Zhuang, Y., Richardson, G. J. *et al.* (1999). Induction of nitric oxide-dependent apoptosis in motor neurons by zinc-deficient superoxide dismutase. *Science*, **286**, 2498–2500.
27. Rakhit, R., Cunningham, P., Furtos-Matei, A., Dahan, S., Qi, X.-F., Crow, J. P. *et al.* (2002). Oxidation-induced misfolding and aggregation of superoxide dismutase and its implications for amyotrophic lateral sclerosis. *J. Biol. Chem.* **277**, 47551–47556.
28. Gruzman, A., Wood, W. L., Alpert, E., Prasad, M. D., Miller, R. G., Rothstein, J. D. *et al.* (2007). Common molecular signature in SOD1 for both sporadic and familial amyotrophic lateral sclerosis. *Proc. Natl Acad. Sci. USA*, **104**, 12524–12529.
29. Ezzi, S. A., Urushitani, M. & Julien, J.-P. (2007). Wild-type superoxide dismutase acquires binding and toxic properties of ALS-linked mutant forms through oxidation. *J. Neurochem.* **102**, 170–178.
30. Kabashi, E., Valdmanis, P. N., Dion, P. & Rouleau, G. A. (2007). Oxidized/misfolded superoxide dismutase-1: the cause of all amyotrophic lateral sclerosis? *Ann. Neurol.* **62**, 553–559.

31. Grad, L. I., Guest, W. C., Yanai, A., Pokrishevsky, E., O'Neill, M. A., Gibbs, E. *et al.* (2011). Intermolecular transmission of superoxide dismutase 1 misfolding in living cells. *Proc. Natl Acad. Sci. USA*, **108**, 16398–16403.
32. Hwang, Y.-M., Stathopulos, P. B., Dimmick, K., Yang, H., Badiei, H. R., Tong, M. S. *et al.* (2010). Nonamyloid aggregates arising from mature copper/zinc superoxide dismutases resemble those observed in amyotrophic lateral sclerosis. *J. Biol. Chem.* **285**, 41701–41711.
33. Munch, C., O'Brien, J. & Bertolotti, A. (2011). Prion-like propagation of mutant superoxide dismutase-1 misfolding in neuronal cells. *Proc. Natl Acad. Sci. USA*, **108**, 3548–3553.
34. Chiti, F. & Dobson, C. M. (2009). Amyloid formation by globular proteins under native conditions. *Nat. Chem. Biol.* **5**, 15–22.
35. Nordlund, A. & Oliveberg, M. (2006). Folding of Cu/Zn superoxide dismutase suggests structural hotspots for gain of neurotoxic function in ALS: parallels to precursors in amyloid disease. *Proc. Natl Acad. Sci. USA*, **103**, 10218–10223.
36. Elam, J. S., Taylor, A. B., Strange, R., Antonyuk, S., Doucette, P. A., Rodriguez, J. A. *et al.* (2003). Amyloid-like filaments and water-filled nanotubes formed by SOD1 mutant proteins linked to familial ALS. *Nat. Struct. Mol. Biol.* **10**, 461–467.
37. Banci, L., Bertini, I., D'Amelio, N., Gaggelli, E., Libralesso, E., Matecko, I. *et al.* (2005). Fully metallated S134N Cu,Zn-superoxide dismutase displays abnormal mobility and intermolecular contacts in solution. *J. Biol. Chem.* **280**, 35815–35821.
38. Danielsson, J., Kurnik, M., Lang, L. & Oliveberg, M. (2011). Cutting off functional loops from homodimeric enzyme superoxide dismutase 1 (SOD1) leaves monomeric β-barrels. *J. Biol. Chem.* **286**, 33070–33083.
39. Evans, D. J. & Searles, D. J. (1994). Equilibrium microstates which generate second law violating steady states. *Phys. Rev. E: Stat. Phys., Plasmas, Fluids, Relat. Interdiscip. Top.* **50**, 1645–1648.
40. Jarzynski, C. (1997). Nonequilibrium equality for free energy differences. *Phys. Rev. Lett.* **78**, 2690–2693.
41. Crooks, G. (1998). Nonequilibrium measurements of free energy differences for microscopically reversible markovian systems. *J. Stat. Phys.* **90**, 1481–1487.
42. Gore, J., Ritort, F. & Bustamante, C. (2003). Bias and error in estimates of equilibrium free-energy differences from nonequilibrium measurements. *Proc. Natl Acad. Sci. USA*, **100**, 12564–12569.
43. Banci, L., Bertini, I., Boca, M., Calderone, V., Cantini, F., Girotto, S. & Vieru, M. (2009). Structural and dynamic aspects related to oligomerization of apo SOD1 and its mutants. *Proc. Natl Acad. Sci. USA*, **106**, 6980–6985.
44. Jonsson, P. A., Ernhill, K., Andersen, P. M., Bergemalm, D., Brännström, T., Gredal, O. *et al.* (2004). Minute quantities of misfolded mutant superoxide dismutase-1 cause amyotrophic lateral sclerosis. *Brain*, **127**, 73–88.
45. Hayward, L. J., Rodriguez, J. A., Kim, J. W., Tiwari, A., Goto, J. J., Cabelli, D. A. *et al.* (2002). Decreased metallation and activity in subsets of mutant superoxide dismutases associated with familial amyotrophic lateral sclerosis. *J. Biol. Chem.* **277**, 15923–15931.
46. Khare, S. D., Caplow, M. & Dokholyan, N. V. (2004). The rate and equilibrium constants for a multistep reaction sequence for the aggregation of superoxide dismutase in amyotrophic lateral sclerosis. *Proc. Natl Acad. Sci. USA*, **101**, 15094–15099.
47. Rumfeldt, J. A., Stathopulos, P. B., Chakrabarrty, A., Lepock, J. R. & Meiering, E. M. (2006). Mechanism and thermodynamics of guanidinium chloride-induced denaturation of ALS-associated mutant Cu,Zn superoxide dismutases. *J. Mol. Biol.* **355**, 106–123.
48. Vassall, K. A., Stathopulos, P. B., Rumfeldt, J. A. O., Lepock, J. R. & Meiering, E. M. (2006). Equilibrium thermodynamic analysis of amyotrophic lateral sclerosis-associated mutant apo Cu,Zn superoxide dismutases. *Biochemistry*, **45**, 7366–7379.
49. Khare, S. D. & Dokholyan, N. V. (2006). Common dynamical signatures of familial amyotrophic lateral sclerosis-associated structurally diverse Cu,Zn superoxide dismutase mutants. *Proc. Natl Acad. Sci. USA*, **103**, 3147–3152.
50. Galaleldeen, A., Strange, R., Whitson, L. J., Antonyuk, S., Narayana, N., Taylor, A. B. *et al.* (2009). Structural and biophysical properties of metal-free pathogenic SOD1 mutants A4V and G93A. *Arch. Biochem. Biophys.* **492**, 40–47.
51. Lindberg, M. J., Normark, J., Holmgren, A. & Oliveberg, M. (2004). Folding of human superoxide dismutase: disulfide reduction prevents dimerization and produces marginally stable monomers. *Proc. Natl Acad. Sci. USA*, **101**, 15893–15898.
52. Potter, S. Z., Zhu, H., Shaw, B. F., Rodriguez, J. A., Doucette, P. A., Sohn, S. H. *et al.* (2007). Binding of a single zinc ion to one subunit of copper-zinc superoxide dismutase apoprotein substantially influences the structure and stability of the entire homodimeric protein. *J. Am. Chem. Soc.* **129**, 4575–4583.
53. Crow, J. P., Sampson, J. B., Zhuang, Y., Thompson, J. A. & Beckman, J. S. (1997). Decreased zinc affinity of amyotrophic lateral sclerosis-associated superoxide dismutase mutants leads to enhanced catalysis of tyrosine nitration by peroxynitrite. *J. Neurochem.* **69**, 1936–1944.
54. Rotilio, G., Calabrese, L., Bossa, F., Barra, D., Agro, A. F. & Mondovi, B. (1972). Properties of the apoprotein and role of copper and zinc in protein conformation and enzyme activity of bovine superoxide dismutase. *Biochemistry*, **11**, 2182–2187.
55. Lippard, S. J., Burger, A. R., Ugurbil, K., Pantoliano, M. W. & Valentine, J. S. (1977). Nuclear magnetic resonance and chemical modification studies of bovine erythrocyte superoxide dismutase: evidence for zinc-promoted organization of the active site structure. *Biochemistry*, **16**, 1136–1141.
56. Kayatekin, C., Zitzewitz, J. A. & Matthews, C. R. (2008). Zinc binding modulates the entire folding free energy surface of human Cu,Zn superoxide dismutase. *J. Mol. Biol.* **384**, 540–555.
57. Nordlund, A., Leinartaite, L., Saraboji, K., Aisenbrey, C., Gröbner, G., Zetterström, P. *et al.* (2009). Functional features cause misfolding of the ALS-provoking enzyme SOD1. *Proc. Natl Acad. Sci. USA*, **106**, 9667–9672.
58. Furukawa, Y. & O'Halloran, T. V. (2005). Amyotrophic lateral sclerosis mutations have the greatest destabilizing

effect on the apo- and reduced form of SOD1 leading to unfolding and oxidative aggregation. *J. Biol. Chem.* **280**, 17266–17274.
59. Feaga, H. A., Maduka, R. C., Foster, M. N. & Szalai, V. A. (2011). Affinity of Cu^{+} for the copper-binding domain of the amyloid-β; peptide of Alzheimer's disease. *Inorg. Chem.* **50**, 1614–1618.
60. Svensson, A.-K. E., Bilsel, O., Kayatekin, C., Adefusika, J. A., Zitzewitz, J. A. & Matthews, C. R. (2010). Metal-free ALS variants of dimeric human Cu, Zn-superoxide dismutase have enhanced populations of monomeric species. *PLoS One*, **5**, e10064.
61. Rodriguez, J. A., Valentine, J. S., Eggers, D. K., Roe, J. A., Tiwari, A., Brown, R. H. & Hayward, L. J. (2002). Familial amyotrophic lateral sclerosis-associated mutations decrease the thermal stability of distinctly metallated species of human copper/zinc superoxide dismutase. *J. Biol. Chem.* **277**, 15932–15937.
62. Rumfeldt, J. A., Lepock, J. R. & Meiering, E. M. (2009). Unfolding and folding kinetics of amyotrophic lateral sclerosis-associated mutant Cu,Zn superoxide dismutases. *J. Mol. Biol.* **385**, 278–298.
63. Ray, S. S., Nowak, R. J., Brown, R. H. & Lansbury, P. T. (2005). Small-molecule-mediated stabilization of familial amyotrophic lateral sclerosis-linked superoxide dismutase mutants against unfolding and aggregation. *Proc. Natl Acad. Sci. USA*, **102**, 3639–3644.
64. Stroppolo, M. E., Malvezzi-Campeggi, F., Mei, G., Rosato, N. & Desideri, A. (2000). Role of the tertiary and quaternary structures in the stability of dimeric copper zinc superoxide dismutases. *Arch. Biochem. Biophys.* **377**, 215–218.
65. Khare, S. D., Caplow, M. & Dokholyan, N. V. (2006). FALS mutations in Cu,Zn superoxide dismutase destabilize the dimer and increase dimer dissociation propensity: a large-scale thermodynamic analysis. *Amyloid*, **13**, 226–235.
66. Vorobjev, Y. N. & Hermans, J. (2001). Free energies of protein decoys provide insight into determinants of protein stability. *Protein Sci.* **10**, 2498–2506.
67. Vorobjev, Y. N. & Hermans, J. (2002). Free energies of protein decoys provide insight into determinants of protein stability. *Protein Sci.* **11**, 994.
68. Lepock, J. R., Frey, H. E. & Hallewell, R. A. (1990). Contribution of conformational stability and reversibility of unfolding to the increased thermostability of human and bovine superoxide dismutase mutated at free cysteines. *J. Biol. Chem.* **265**, 21612–21618.
69. Doucette, P. A., Whitson, L. J., Cao, X., Schirf, V., Demeler, B., Valentine, J. S. *et al.* (2004). Dissociation of human copper-zinc superoxide dismutase dimers using chaotrope and reductant. *J. Biol. Chem.* **279**, 54558–54566.
70. Ding, F. & Dokholyan, N. V. (2008). Dynamical roles of metal ions and the disulfide bond in Cu, Zn superoxide dismutase folding and aggregation. *Proc. Natl Acad. Sci. USA*, **105**, 19696–19701.
71. Ahmed, M. S., Hung, W.-Y., Zu, J. S., Hockberger, P. & Siddique, T. (2000). Increased reactive oxygen species in familial amyotrophic lateral sclerosis with mutations in SOD1. *J. Neurol. Sci.* **176**, 88–94.
72. Alvarez, B., Demicheli, V., Durán, R., Trujillo, M., Cerveñansky, C., Freeman, B. A. & Radi, R. (2004). Inactivation of human Cu,Zn superoxide dismutase by peroxynitrite and formation of histidinyl radical. *Free Radical Biol. Med.* **37**, 813–822.
73. Lipton, S. A., Gu, Z. & Nakamura, T. (2007). Inflammatory mediators leading to protein misfolding and uncompetitive/fast off-rate drug therapy for neurodegenerative disorders. *Int. Rev. Neurobiol.* **82**, 1–27.
74. Lamb, A. L., Torres, A. S., O'Halloran, T. V. & Rosenzweig, A. C. (2001). Heterodimeric structure of superoxide dismutase in complex with its metallochaperone. *Nat. Struct. Biol.* **8**, 751–755.
75. Leinartaite, L., Saraboji, K., Nordlund, A., Logan, D. T. & Oliveberg, M. (2010). Folding catalysis by transient coordination of Zn^{2+} to the Cu ligands of the ALS-associated enzyme Cu/Zn superoxide dismutase 1. *J. Am. Chem. Soc.* **132**, 13495–13504.
76. Sotomayor, M. & Schulten, K. (2007). Single-molecule experiments *in vitro* and *in silico*. *Science*, **316**, 1144–1148.
77. Carrion-Vazquez, M., Li, H., Lu, H., Marszalek, P. E., Oberhauser, A. F. & Fernandez, J. M. (2003). The mechanical stability of ubiquitin is linkage dependent. *Nat. Struct. Biol.* **10**, 738–743.
78. Irback, A., Mitternacht, S. & Mohanty, S. (2005). Dissecting the mechanical unfolding of ubiquitin. *Proc. Natl Acad. Sci. USA*, **102**, 13427–13432.
79. Imparato, A. & Pelizzola, A. (2008). Mechanical unfolding and refolding pathways of ubiquitin. *Phys. Rev. Lett.* **100**, 158104.
80. Jorgensen, W., Maxwell, D. & Tirado-Rives, J. (1996). Development and testing of the OPLS all-atom force field on conformational energetics and properties of organic liquids. *J. Am. Chem. Soc.* **118**, 11225–11236.
81. Kaminski, G. A. & Friesner, R. A. (2001). Evaluation and reparametrization of the OPLS-AA force field for proteins via comparison with accurate quatum chemical calculations with peptides. *J. Phys. Chem. B*, **105**, 6474–6487.
82. Bjelkmar, P., Larsson, P., Cuendet, M. A., Hess, B. & Lindahl, E. (2010). Implementation of the CHARMM force field in GROMACS: analysis of protein stability effects from correlation maps, virtual interaction sites, and water models. *J. Chem. Theo. Comp.* **6**, 459–466.
83. Onufriev, A., Bashford, D. & Case, D. (2004). Exploring protein native states and large-scale conformational changes with a modified generalized Born model. *Proteins SFG*, **55**, 383–394.
84. Hess, B., Bekker, H., Berendsen, H. J. C. & Fraaije, J. G. E. M. (1997). LINCS: a linear constraint solver for molecular simulations. *J. Comp. Chem.* **18**, 1463–1472.
85. Lemkul, J. A. & Bevan, D. R. (2010). Assessing the stability of Alzheimer's amyloid protofibrils using molecular dynamics. *J. Phys. Chem. B*, **114**, 1652–1660.
86. Kim, T., Rhee, A. & Yip, C. M. (2006). Force-induced insulin dimer dissociation: a molecular dynamics study. *J. Am. Chem. Soc.* **128**, 5330–5331.
87. Gerini, M. F., Roccatano, D., Baciocchi, E. & Nola, A. D. (2003). Molecular dynamics simulations of lignin peroxidase in solution. *Biophys. J.* **84**, 3883–3893.
88. Lv, S., Dudek, D. M., Cao, Y., Balamurali, M. M., Gosline, J. & Li, H. (2010). Designed biomaterials to mimic the mechanical properties of muscles. *Nature*, **465**, 69–73.

89. Cashman, N. R., Plotkin, S. S. & Guest, W. C. (2010). US patent 12/574,637: methods and systems for predicting misfolded protein epitopes; 9/16/10.
90. Yao, Y., Harrison, C. B., Freddolino, P. L., Schulten, K. & Mayer, M. L. (2008). Molecular mechanism of ligand recognition by NR3 subtype glutamate receptors. *EMBO J.* **27**, 2158–2170.
91. Phillips, J. C., Braun, R., Wang, W., Gumbart, J., Tajkhorshid, E., Villa, E. *et al.* (2005). Scalable molecular dynamics with NAMD. *J. Comp. Chem.* **26**, 1781–1802.
92. Seeber, M., Cecchini, M., Rao, F., Settanni, G. & Caflisch, A. (2007). Wordom: a program for efficient analysis of molecular dynamics simulations. *Bioinformatics*, **23**, 2625–2627.
93. DeLano, W. L. (2002). The PyMOL molecular graphics system, http://www.pymol.org.
94. Kumar, S., Rosenberg, J. N., Bouzida, D., Swendsen, R. H. & Kollman, P. A. (1992). The weighted histogram analysis method for free-energy calculations on biomolecules. I. The method. *J. Comput. Chem.* **13**, 1011–1021.
95. Patey, G. N. & Valleau, J. P. (1973). The free energy of spheres with dipoles: Monte Carlo with multistage sampling. *Chem. Phys. Lett.* **21**, 297–300.
96. Torrie, G. M. & Valleau, J. P. (1974). Monte Carlo free energy estimates using non-Boltzmann sampling: application to the sub-critical Lennard-Jones fluid. *Chem. Phys. Lett.* **28**, 578–581.
97. Torrie, G. M. & Valleau, J. P. (1977). Nonphysical sampling distributions in Monte Carlo free-energy estimation: umbrella sampling. *J. Comput. Phys.* **23**, 187–199.

Mechanical probes of SOD1 predict systematic trends in metal and dimer affinity of ALS-associated mutants (Supplementary Content)

Atanu Das * **and Steven S. Plotkin** *

*Department of Physics and Astronomy, University of British Columbia, Vancouver, Canada

Supplemental Figures

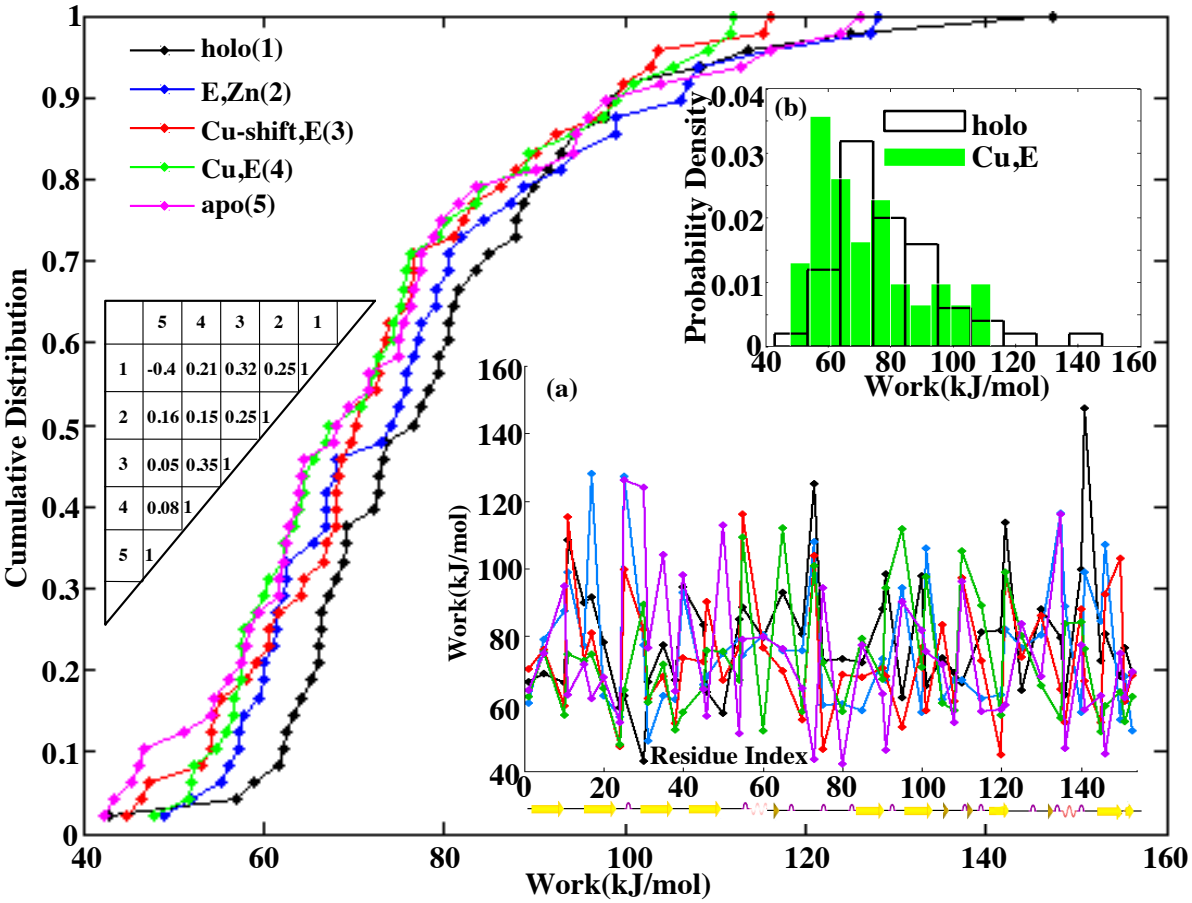

	5	4	3	2	1
1	-0.4	0.21	0.32	0.25	1
2	0.16	0.15	0.25	1	
3	0.05	0.35	1		
4	0.08	1			
5	1				

Fig. S1. The effect of metal depletion on the mechanical stability of SOD1. (Inset panel a) Mechanical profiles of holo SOD1, (E,Zn) SOD1, (Cu,E) SOD1, and Zn-depleted SOD1 with the Cu ion shifted from its putative position to that of the Zn (Cu-shift,E), which is near the location of the Cu observed in the crystal structure of PDB 2R27. Profiles are color-coded according to the legend in the upper left. The effect of metal depletion modulates the entire mechanical stability profile. Work values for individual residues are given in Table S5 of the Supplementary Content. (Inset b) Probability distributions of mechanical stability for holo and (Cu,E) variants. This representation shows that the distributions are indeed different, however there is significant overlap, which along with the necessity of binning the data to construct the histogram, makes the differences difficult to quantify. (Main Panel) Cumulative histograms of the above SOD1 variants. The cumulative histogram requires no binning, and simply rank orders and accumulates the work values. Using this representation, discrepancies between work profiles most clearly emerge. The mechanical stability of the SOD1 variants can be rank ordered, strongest to weakest, as holo, (E,Zn), (Cu-shift,E), and (Cu,E). The distribution of apo SOD1 is broadened compared to (Cu,E) SOD1, but not overall weakened. Also shown in the main panel is a correlation matrix resulting from a pairwise comparison of the work values for all pairings of SOD1 variants. The profiles do not correlate, again supporting the notion that metal depletion modulates the entire mechanical stability profile.

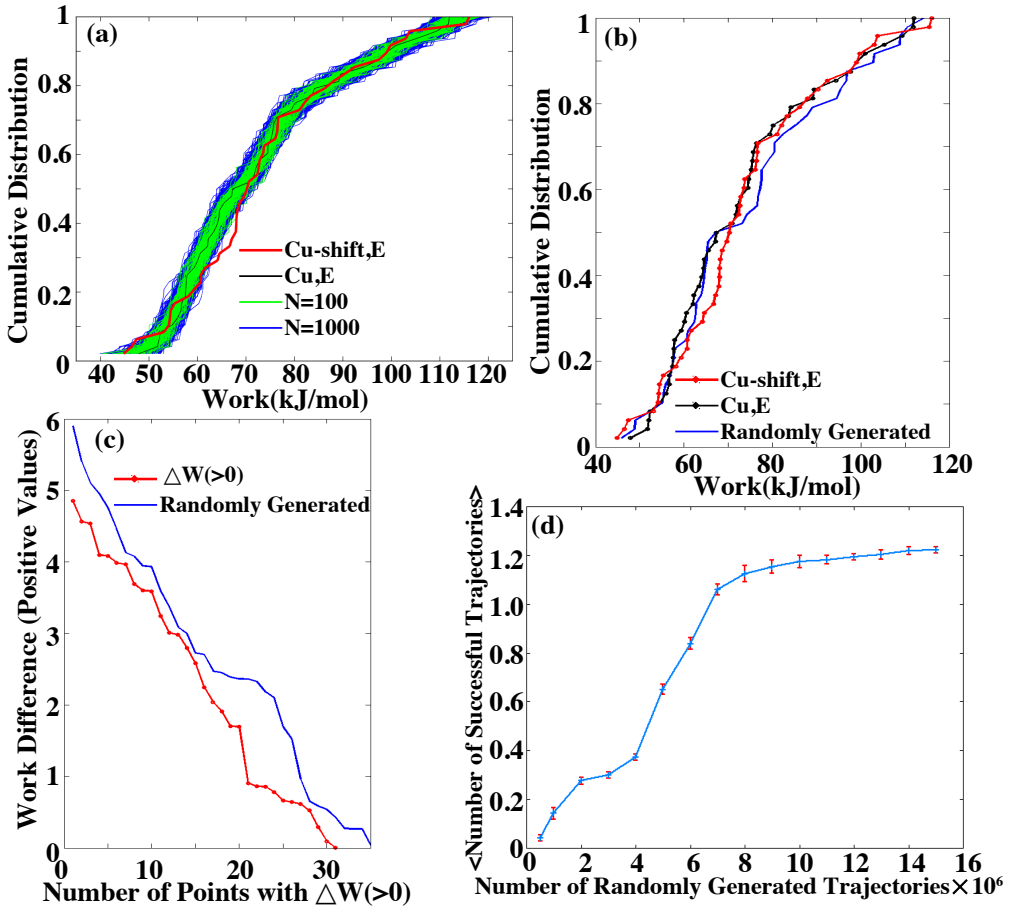

Fig. S2. (a) Statistical significance test between (Cu,E) and (Cu-shift,E) cumulative distributions. The black curve denotes the (Cu,E) profile, and the red curve denotes the (Cu-shift,E) profile. The collection of green lines corresponds to 100 randomly-generated cumulative distributions in the following way: starting from the (Cu,E) work values, gaussian noise with zero mean and standard deviation σ = 2.7 kJ/mol is added to each work value. The resulting collection of work values are then rank-ordered to generate a cumulative distribution, and this process is then repeated N times. The collection of blue lines corresponds to $N = 1000$. For large enough N, one will begin to find outlying cumulative distributions which deviate as much or more than a given trial distribution, here (Cu-shift,E). An example of such an outlier is shown in panel (b). In this case, the number of positive deviations (differences in work value) between the red and black curves in panel (a) are recorded (31), along with their work values, which are themselves rank ordered largest to smallest and plotted in figure (c). An outlier at least as extreme as (Cu-shift,E) must have a set of positive work deviations such that the corresponding curve lies above the red curve in panel (c). In this case the randomly generated outlier has 36 positive deviations in work, 31 of which are larger than those between (Cu-shift,E) and (Cu,E) variants. The number of randomly generated trajectories is increased, until the mean number of successful trajectories, corresponding to the criterion in panel (c), exceeds unity. A plot of the mean number of successful trajectories as a function of N is given in panel (d). The statistical significance p of a given trajectory is then given as $p = 1/N_1$, where N_1 is the number of randomly generated trajectories that give an expectation value of unity for the number of successfully-generated outliers. In this case, the statistical significance of (Cu-shift,E) is about $1/(7 \times 10^6)$, or about 1.4×10^{-7}.

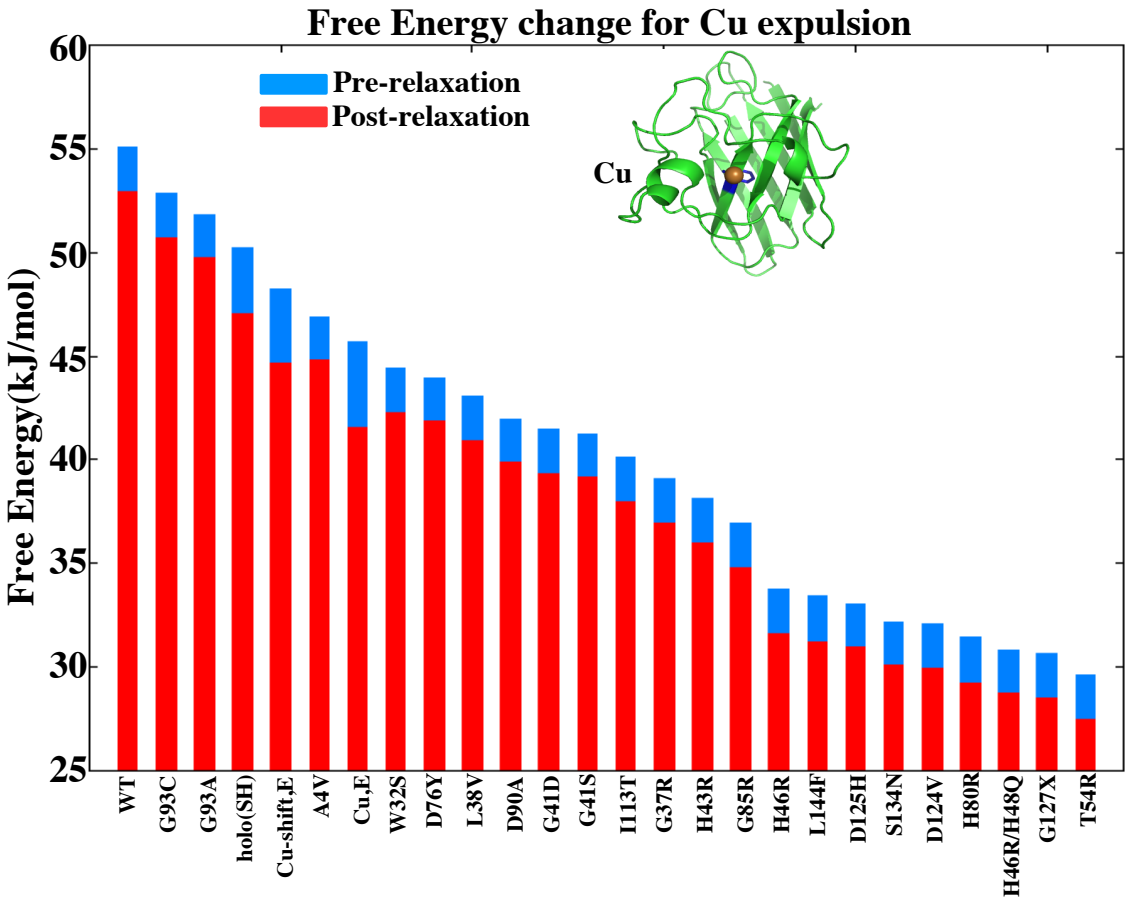

Fig. S3. Free energy change for Cu expulsion, for WT SOD1 along with several mutants and post-translationally modified variants. The heights of the blue bars indicate the corresponding free energies of metal binding before conformational relaxation of the protein in the unbound state. Red bar heights indicate the corresponding free energies of binding after relaxation of the protein in the unbound state. A decrease in free energy value is observed for all the proteins.

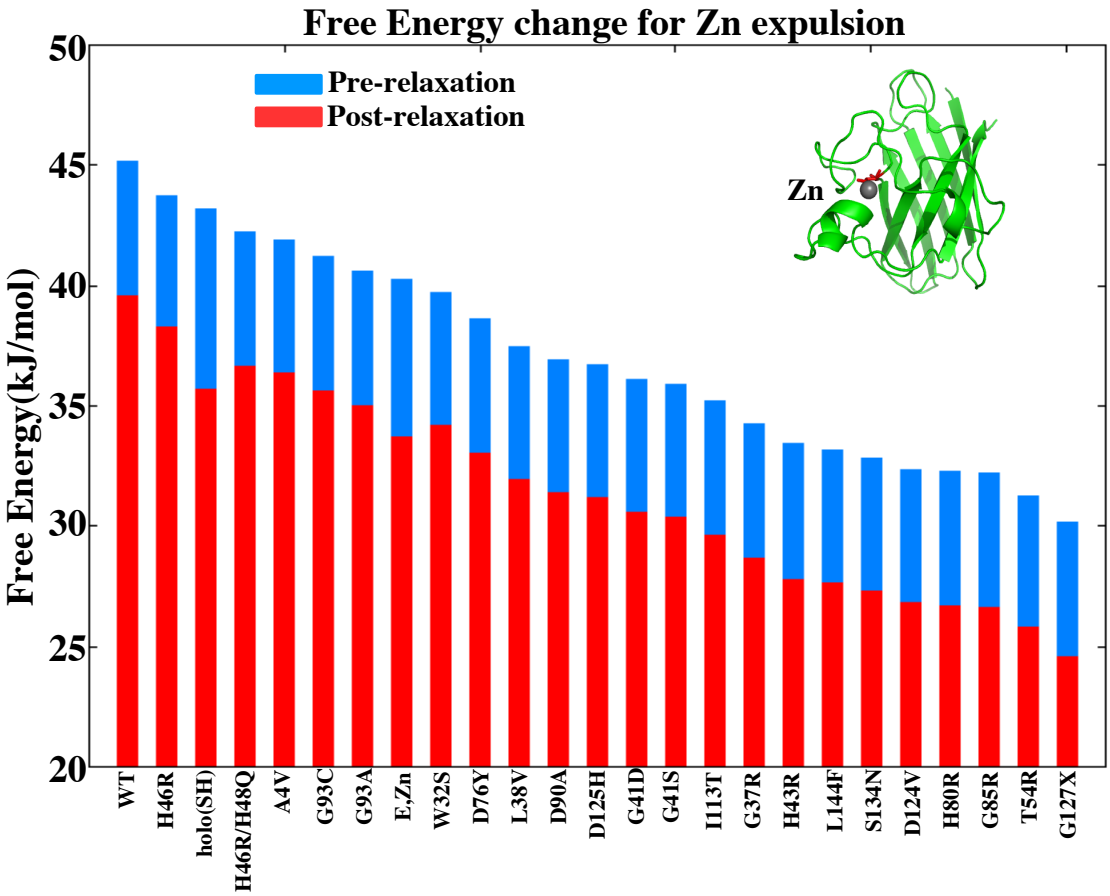

Fig. S4. Free energy change for Zn expulsion, for WT SOD1 along with several mutants and post-translationally modified variants. The heights of the blue bars indicate the corresponding free energies of metal binding before conformational relaxation of the protein in the unbound state. Red bar heights indicate the corresponding free energies of binding after relaxation of the protein in the unbound state.

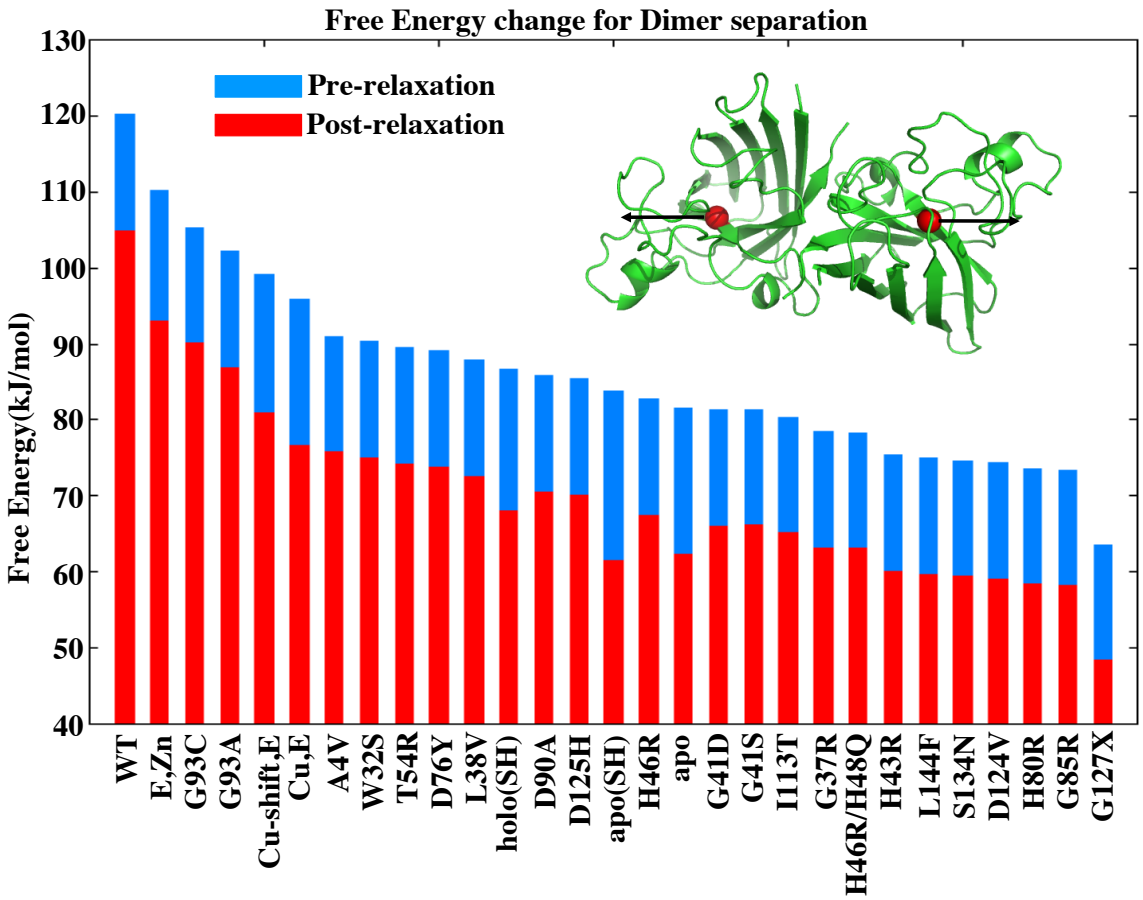

Fig. S5. Free energy change for dimer separation, for WT holo SOD1 along with several mutants and post-translationally modified variants. All mutants plotted here are taken in the holo state. The heights of the blue bars indicate the corresponding free energy to monomerize the dimer before conformational relaxation of both proteins in the unbound state. Red bar heights indicate the corresponding free energies of binding after conformational relaxation of both protein in the monomerized state.

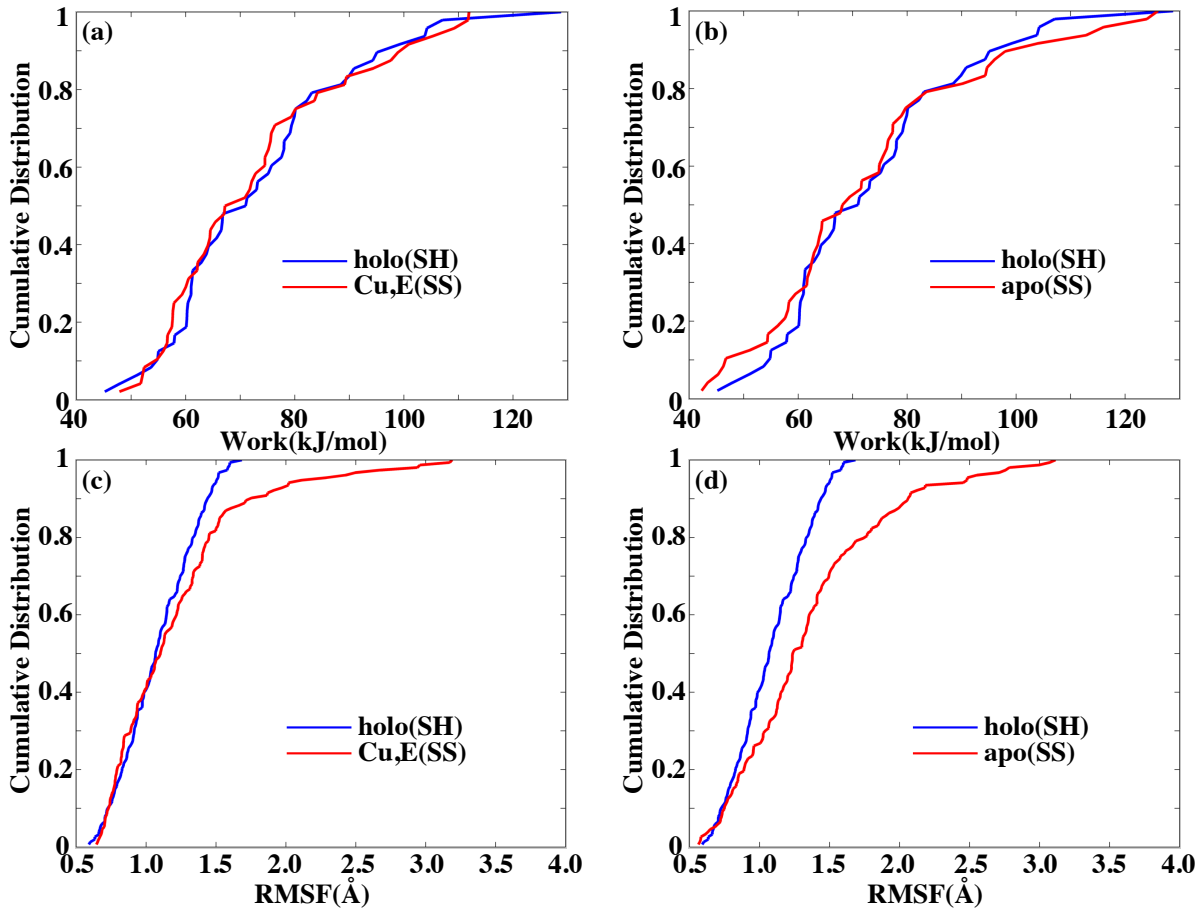

Fig. S6. Loss of Zn is at least as destabilizing to SOD1 mechanical stability as disulfide reduction. Panel (a) gives the cumulative distribution of the work profiles for holo(SH) and Cu,E(SS) SOD1 variants, which shows that Cu,E(SS) SOD1 has marginally weaker mechanical stability than holo(SH) SOD1 (p = 1.4e-7). This trend is also observed in the cumulative distribution of the equilibrium fluctuations of the holo(SH) and Cu,E(SS) variants (Panel (c)), where Cu,E(SS) shows marginally larger fluctuations. Panel (b) compares cumulative distributions of work profiles for holo(SH) and apo(SS) SOD1, showing apo(SS) SOD1 is marginally weaker mechanically (p = 3e-8). The cumulative distribution of equilibrium fluctuations of these two variants (panel d) also shows that apo(SS) SOD1 has more significant dynamics in the native state.

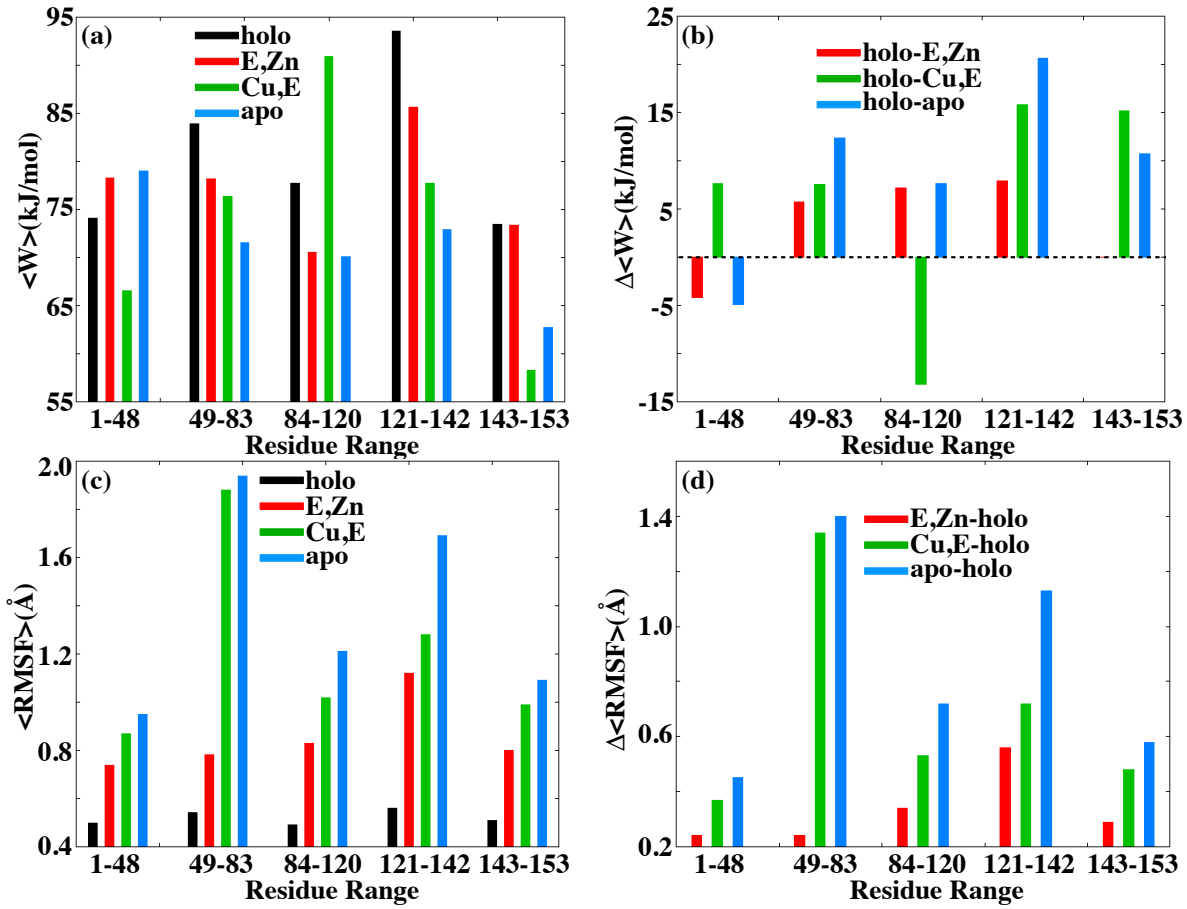

Fig. S7. Zn-binding and electrostatic loops (ZBL and ESL) show decreased mechanical rigidity and increased dynamic mobility upon metal release. The SOD1 sequence is divided into 5 different regions: the region N-terminal to the ZBL (residues 1-48), the ZBL (residues 49-83), the middle region of sequence between the ZBL and ESL (residues 84-120), the ESL (residues 121-142), and the C-terminal region after the ESL (residues 143-153). Panel (a) gives the average work values (as calculated by pulling to 5Å) for those regions, for holo, (E,Zn), (Cu,E) and apo SOD1 variants. Panel (b) gives the difference in average work values of those 5 regions in the various metal-deficient forms of SOD1 from holo SOD1 (e.g. $\langle W \rangle_{holo} - \langle W \rangle_{apo}$). This shows that metal loss systematically destabilizes the ZBL and ESL; other regions of the proteins show less systematic trends. Panel (c) gives the root mean squared fluctuations (RMSF) averaged over the above 5 regions, and panel (d) gives the difference in RMSF of those 5 regions in the various metal-deficient forms of SOD1 from holo SOD1 (e.g. $\langle RMSF \rangle_{apo} - \langle RMSF \rangle_{holo}$). This recapitulates the mechanical stability assay: metal loss systematically increases dynamic fluctuations in the ZBL and ESL. Other regions show weaker trends in dynamic fluctuations.

Supplemental Tables

Table S1. Free energy of Cu, Zn expulsion and Dimer separation (kJ/mol)

SOD1 variants	Cu^{2+}	Cu^{1+}	Zn^{2+}	Dimer
WT	52.9	26.4	39.6	104.9
holo(SH)	47.1	23.5	35.7	68.1
(Cu-shift,E)	44.6	22.3	-	80.9
(Cu,E)	41.5	20.7	-	76.6
(E,Zn)	-	-	33.7	93.1
(E,Zn)(SH)	-	-	32.6	66.7
apo(SH)	-	-	-	61.5
apo	-	-	-	62.3
G93C	50.7	25.3	35.6	90.2
G93A	49.7	24.8	35.0	86.8
A4V	44.8	22.4	36.4	75.7
W32S	42.3	21.2	34.1	74.9
D76Y	41.8	20.9	33.0	73.8
L38V	40.9	20.4	31.9	72.6
D90A	39.9	19.9	31.4	70.5
G41D	39.3	19.6	30.5	66.0
G41S	39.1	19.5	30.4	66.1
I113T	38.0	19.0	29.6	65.1
G37R	36.9	18.4	28.7	63.2
H43R	35.9	17.9	27.8	60.1
G85R	34.8	17.3	26.6	58.2
H46R	31.6	15.8	38.2	67.4
L144F	31.2	15.6	27.6	59.6
D125H	30.9	15.4	31.2	70.1
S134N	30.1	15.0	27.3	59.5
D124V	30.0	14.9	26.8	59.0
H80R	29.2	14.6	26.7	58.3
H46R/H48Q	28.7	14.3	36.6	63.0
G127X	28.5	14.2	24.6	48.3
T54R	27.4	13.7	25.8	74.1
(E,Zn)H46R	-	-	-	60.2
(E,Zn)H46R/H48Q	-	-	-	58.9
apoA4V	-	-	-	47.1
apoG37R	-	-	-	51.6
apoL38V	-	-	-	48.1
apoG41S	-	-	-	47.1
apoH46R	-	-	-	49.1
apoT54R	-	-	-	48.5
apoD76Y	-	-	-	49.1
apoG85R	-	-	-	47.9
apoD90A	-	-	-	50.1
apoG93C	-	-	-	50.9
apoI113T	-	-	-	46.9
apoD124V	-	-	-	47.0
apoD125H	-	-	-	48.0
apoG127X	-	-	-	44.2
apoS134N	-	-	-	48.1
apoL144F	-	-	-	49.1

Table S2. Free energy change for metal expulsion and dimer separation (kJ/mol) - thermodynamic cycle (see Figure 4, main text)

Metal	ΔF_1^{constr}	$-\Delta F_2^{relax}$	ΔF_3^{constr}	$-\Delta F_4^{relax}$
WT(Cu)	55.0	2.1	53.5	0.8
WT(Zn)	45.1	5.5	41.4	1.9
Cu,E(Cu)	45.6	4.1	43.4	1.7
E,Zn(Zn)	40.2	6.5	36.6	3.0
A4V(Cu)	46.9	2.1	45.5	0.9
A4V(Zn)	41.9	5.5	38.6	2.1
G93A(Cu)	51.8	2.1	50.5	0.9
G93A(Zn)	40.6	5.6	37.4	2.2
Dimer	ΔF_1^{constr}	$-\Delta F_2^{relax}$	ΔF_3^{constr}	$-\Delta F_4^{relax}$
WT	120.1	15.2	111.7	6.6
Cu,E	95.8	19.2	86.0	9.2
E,Zn	110.2	17.1	100.2	7.2
A4V	91.0	15.3	84.9	8.9
G93A	102.1	15.3	93.7	7.1

Table S3. Correlation between Work and RMSF of SOD1 variants

Correlation	holo	E,Zn	Cu-shift,E	Cu,E	apo	holo(SH)	apo(SH)
r	0.06	−0.02	0.06	0.08	0.01	0.07	4.7×10^{-5}
p	0.69	0.89	0.66	0.57	0.94	0.61	0.99

Table S4. Correlation table of work values for different variants of SOD1

r† / p	holo	E,Zn	Cu-shift,E	Cu,E	apo	holo(SH)	apo(SH)
holo	1	0.25	0.32	0.21	-0.37	-0.02	-0.16
E,Zn	0.09	1	0.25	0.15	0.16	-0.06	-0.07
Cu-shift,E	0.03	0.09	1	0.35	0.05	0.17	0.05
Cu,E	0.15	0.30	0.01	1	0.08	0.13	0.07
apo	0.01	0.26	0.74	0.57	1	0.30	0.51
holo(SH)	0.91	0.68	0.26	0.38	0.04	1	0.33
apo(SH)	0.27	0.63	0.72	0.62	0.0002	0.02	1

†r indicates the correlation coefficient between work profiles of different SOD1 variants, and p indicates the statistical significance of the correlation coefficient.

Table S5. Mechanical work values of WT SOD1 variants - the values reported in the table depict the work in kJ/mol needed to pull a particular residue up to 5 Å.

Res.Ind.	holo	(E,Zn)	(Cu-shift,E)	(Cu,E)	apo	holo(SH)	apo(SH)
1	66.3	60.1	70.2	62.2	63.9	60.1	60.3
5	68.8	79.0	76.0	75.1	74.9	77.5	88.9
10	66.1	87.4	59.3	56.7	94.6	79.4	81.2
11	108.4	98.9	115.3	74.5	62.5	63.8	59.5
15	89.9	77.1	72.8	72.8	71.5	79.1	68.8
17	91.5	128.0	81.0	74.5	61.6	61.2	45.1
20	78.2	62.4	64.5	64.5	67.7	103.8	60.6
24	58.8	56.0	47.4	47.8	54.4	48.0	56.7
25	62.3	127.3	99.8	64.0	126.0	62.9	87.3
30	42.9	77.3	82.0	89.4	124.0	75.7	113.4
31	66.3	48.9	61.5	60.5	76.5	60.2	55.9
35	77.3	62.2	68.0	71.7	104.0	66.7	84.1
38	67.1	61.2	54.1	52.4	63.5	64.2	64.7
40	94.4	92.9	73.5	57.4	98.0	83.1	91.5
45	83.4	65.5	72.3	64.4	64.3	78.0	68.1
46	63.3	68.0	90.2	75.7	56.2	71.0	66.8
50	57.0	74.9	67.0	75.5	112.8	78.0	78.2
54	85.0	78.9	76.4	67.0	51.1	45.2	71.6
55	88.6	74.2	116.0	109.2	78.9	94.3	72.6
60	79.5	80.4	76.5	52.1	79.7	90.8	58.4
65	92.9	75.7	69.6	111.9	76.2	107.0	83.2
70	80.5	75.7	55.2	57.6	64.4	57.8	95.8
73	125.0	108.0	103.7	100.8	43.4	55.0	60.8
75	72.8	59.5	46.4	72.1	94.3	53.6	71.4
80	73.1	60.0	68.6	57.6	42.3	73.0	72.1
85	72.1	57.9	67.9	79.3	77.3	65.6	70.8
90	87.9	73.1	70.5	67.2	62.9	128.8	74.4
91	98.4	66.9	68.0	94.3	46.2	60.2	61.3
95	61.7	94.2	53.0	111.7	90.1	89.8	82.9
100	97.8	57.3	76.6	70.8	81.6	88.4	87.4
101	65.3	106.0	58.1	97.6	75.5	61.2	40.2
105	73.5	61.3	83.3	60.0	71.6	95.0	63.5
108	69.2	67.0	60.6	57.8	54.3	51.0	40.2
110	66.2	67.0	97.3	105.2	96.0	73.2	86.6
115	81.1	61.5	72.6	89.1	57.6	82.2	72.7
120	81.6	62.6	44.7	56.6	58.1	66.8	101.1
121	113.6	81.9	99.0	98.9	59.5	66.5	66.7
125	64.1	76.6	73.7	80.1	83.5	75.1	82.8
130	87.9	80.4	86.1	65.4	68.1	80.1	103.1
135	79.4	116.2	64.1	55.8	116.0	104.2	85.1
136	62.5	88.8	54.4	83.6	46.7	61.0	70.2
140	99.7	57.3	87.9	84.1	77.4	79.9	92.1
141	147.3	98.9	66.6	76.3	58.3	54.8	56.8
145	72.8	84.4	54.3	51.7	62.2	71.2	76.2
146	80.5	107.0	92.4	59.3	45.3	61.0	61.2
150	68.1	55.3	103.0	63.3	74.8	99.2	80.2
151	76.6	68.0	60.6	54.7	61.7	58.0	66.1
153	69.0	52.1	68.2	62.1	69.5	60.4	60.3

Table S6. Finite sample size correction of Jarzynski equality (energies are in kJ/mol)

Residue Index	$\langle W \rangle_N$	$\overline{W}_{dis}$	$\overline{W}_{dis2}$	$\alpha(\overline{W}_{dis})$	$\alpha(\overline{W}_{dis2})$	ΔF_{J}	ΔF
10	56.24	0.110	1.33	−0.804	0.25	56.13	55.50
17	80.27	0.108	1.13	−0.756	0.28	80.16	77.55